JGR Atmospheres

RESEARCH ARTICLE
10.1029/2024JD042633

Key Points:

- Annual behavior of the global electric circuit (GEC) intensity is hard to infer from measurements; variations at specific UTC hours may differ from their diurnal mean
- Electric field data from Vostok station indicate that diurnal mean GEC intensity is highest in boreal summer and lowest in austral summer
- The seasonal cycle of insolation can provide a physical interpretation for the Vostok electric field variation, including its subtle details

Supporting Information:

Supporting Information may be found in the online version of this article.

Correspondence to:

N. N. Slyunyaev,
slyunyaev.n@ipfran.ru

Citation:

Slyunyaev, N. N., Sarafanov, F. G., Ilin, N. V., Mareev, E. A., Volodin, E. M., Frank-Kamenetsky, A. V., & Williams, E. R. (2025). The seasonal variation of the direct current global electric circuit: 1. A new analysis based on long-term measurements in Antarctica. *Journal of Geophysical Research: Atmospheres*, *130*, e2024JD042633. https://doi.org/10.1029/2024JD042633

Received 3 OCT 2024
Accepted 15 FEB 2025

The Seasonal Variation of the Direct Current Global Electric Circuit: 1. A New Analysis Based on Long-Term Measurements in Antarctica

Nikolay N. Slyunyaev[1], Fedor G. Sarafanov[1], Nikolay V. Ilin[1], Evgeny A. Mareev[1], Evgeny M. Volodin[2], Alexander V. Frank-Kamenetsky[3], and Earle R. Williams[4]

[1]Institute of Applied Physics, Russian Academy of Sciences, Nizhny Novgorod, Russia, [2]Institute of Numerical Mathematics, Russian Academy of Sciences, Moscow, Russia, [3]Arctic and Antarctic Research Institute, St. Petersburg, Russia, [4]Parsons Laboratory of the Department of Civil and Environmental Engineering, Massachusetts Institute of Technology, Cambridge, MA, USA

Abstract It has long been noted that the seasonal behavior of the global electric circuit (GEC) is difficult to reliably determine from measurements of atmospheric electrical parameters, largely owing to prominent annual cycles of aerosols affecting the conductivity in most continental locations. Here we discuss earlier studies in this direction and present further analysis of this problem using the results of potential gradient (PG) measurements at the Vostok station in Antarctica during 2006–2020. Collected at the high and remote Antarctic Plateau, Vostok PG values form a unique continuous data set indicating the variation of atmospheric electricity on different timescales; on the annual timescale the uniformity and consistency of the data turn out to be especially important (in particular, seasonal behavior of GEC parameters at specific UTC hours may be substantially different from the respective diurnal mean variation). PG measurements at Vostok indicate the highest and lowest values of the diurnal mean GEC intensity during the Northern Hemisphere summer and winter, respectively; this variation generally agrees with the available results of air—Earth current measurements. The seasonal variation of the GEC has been previously linked to the annual cycle of insolation; our findings further support this relationship, as it can provide a physical explanation not only for the summer PG maximum observed at Vostok but also for a small local minimum inside this maximum. The dominance of the Northern Hemisphere in the resulting variation is apparently related to the latitudinally asymmetrical distribution of land over the Earth's surface.

Plain Language Summary The global electric circuit (GEC) is an overarching concept in atmospheric electricity, according to which electrified clouds generate a distribution of electromagnetic fields all over the Earth. Notwithstanding that the annual cycle of summer and winter is the largest cause of atmospheric variations on Earth, the seasonal variation of the GEC is still not reliably known, since measurements of atmospheric electrical parameters do not yield a comprehensive answer. Here we discuss earlier studies in this direction and further analyze this problem using the results of electric field measurements at the Vostok station in Antarctica. The Vostok station is situated at the high and remote Antarctic Plateau, which makes it a very clean location, convenient for atmospheric electricity research. After a careful discussion of different data sets we conclude that the actual GEC intensity is likely to be at a maximum during the Northern Hemisphere summer and at a minimum during the Northern Hemisphere winter. Such behavior can be given a clear physical interpretation in terms of the annual cycle of insolation at different latitudes and the distribution of land and ocean across the two hemispheres (these factors influence the intensity of convection, linked to charge separation inside electrified clouds).

1. Introduction

The global electric circuit (GEC) is an overarching concept in atmospheric electricity, according to which thunderstorms and, more generally, electrified clouds generate a distribution of electromagnetic fields all over the Earth (see, e.g., Rycroft et al., 2008; Williams, 2009; Williams & Mareev, 2014). In this connection the global distribution of quasi-stationary electric fields and currents maintained by charge separation inside electrified clouds is called the direct current (DC) GEC, while global electromagnetic resonances excited in the Earth—ionosphere cavity by lightning comprise the so-called alternating current (AC) GEC.

This study will concentrate on the DC GEC (hereafter we shall omit the prefix "DC"), which can be roughly described as follows: Charge separation inside thunderstorms and electrified shower clouds (ESCs) drives the electric current upward, then the ionosphere (which is far more conductive than the lower atmosphere) brings this current to fair-weather regions, where it flows downward, and the Earth's surface (whose conductivity is also much greater than that of the surrounding air) completes the circuit. In this way regions occupied by electrified clouds become linked to fair-weather regions within a global electrical network (a hypothesis first proposed by Wilson, 1921).

The concept of the GEC implies, in particular, that both the Earth's surface and the lower ionosphere are nearly equipotential, hence the potential difference between them (maintained by electrified clouds all over the Earth) must be more or less the same even at remote locations. This potential difference is called the ionospheric potential (IP), and it is arguably the most natural characteristic of the GEC intensity. However, determining the IP from measurements requires knowing the vertical profile of the potential gradient (PG) up to at least several kilometers above sea level (Markson, 2007; Mühleisen, 1971), which requires expensive aircraft or balloon soundings.

On the other hand, one can often estimate the GEC intensity from measuring the fair-weather PG at the Earth's surface. A major problem with this approach is the dependence of the surface PG on local factors, in particular on local conductivity perturbations (e.g., due to radon or aerosols). To eliminate such local effects, one must perform measurements at a clean location. Notable examples of such campaigns are PG measurements on board the Carnegie ship in the Pacific, Atlantic, and Indian Oceans in 1915–1921 and 1928–1929 (Ault & Mauchly, 1926; Torreson et al., 1946) and on board the Maud ship in the Arctic Ocean in 1922–1925 (Sverdrup, 1926); more recent observations include PG measurements at the Vostok station, located at the high and remote Antarctic Plateau (78.5°S, 106.9°E, 3,488 m above sea level; see, e.g., Burns et al., 2012, 2017).

In addition to the PG, it is also possible to measure the fair-weather air—Earth current density, which is not affected by local conductivity perturbations and, by inference, should be more representative of the GEC intensity in most continental locations. However, precise measurements of this quantity are rather difficult, and little air—Earth current data are available (Adlerman & Williams, 1996; Anisimov & Shikhova, 2014; Cobb & Phillips, 1962; Gherzi, 1967; Harrison & Ingram, 2005; Harrison & Nicoll, 2008; Hogg, 1950; Retalis, 1991; Scrase, 1933).

During the Carnegie and Maud campaigns in the early twentieth century it was noted that the dependence of the mean fair-weather PG on universal time of day (i.e., on the UTC hour) looks nearly the same at different locations (Mauchly, 1921, 1923; Sverdrup, 1926); this dependence is now referred to as the Carnegie curve. Later analysis has shown that the shape of the diurnal variation of global thunderstorm activity is visually similar to that of the Carnegie curve (Whipple, 1929a; Whipple & Scrase, 1936), which has become an important piece of evidence supporting Wilson's hypothesis about the GEC. Note that in reality electrified clouds without lightning are equally important for maintaining the GEC (Wilson, 1921), and thunderstorms alone would produce a diurnal variation with at least twice as large a peak-to-peak amplitude (e.g., Mach et al., 2011; Williams & Heckman, 1993); however, global thunderstorm activity still should, to a certain extent, reflect the distribution of GEC generators.

Although the classical Carnegie curve, strictly speaking, does not represent the true mean diurnal variation of the DC GEC owing to the substantial seasonal variability of the GEC and nonuniform seasonal sampling of the Carnegie data (see Burns et al., 2017), more or less similar variations were later obtained on the basis of IP soundings (Markson, 1986; Mühleisen, 1977) and PG measurements in other locations (e.g., Harrison, 2003).

Since the intensity of the GEC is determined by contributions to the IP from electrified clouds all over the globe, and considering that such clouds are generally associated with deep convection, it is not surprising that parameters of the GEC reflect changes in global weather and climate. Research over the past 10 years has shown that the GEC variation contains clear patterns related to modes of atmospheric variability which affect convection in the tropics, namely to the El Niño—Southern Oscillation (Harrison et al., 2022; Lavigne et al., 2017; Slyunyaev, Frank-Kamenetsky, et al., 2021) and the Madden–Julian oscillation (Kozlov et al., 2023; Tacza et al., 2022). These patterns have been identified both in IP simulations with models of atmospheric dynamics and in actual fair-weather PG measurements.

In view of these findings, it would be natural to expect that the GEC variation also reflects the seasonal cycle of summers and winters, which can be regarded as the most pronounced mode of atmospheric variability on Earth.

One could anticipate having some universal annual behavior of the main GEC parameters, similarly to the Carnegie curve in the case of their diurnal variation. It turns out, however, that despite all the existing measurements of the IP, fair-weather PG, and fair-weather air—Earth current, the seasonal variation of the GEC is still not reliably known, as different data sets imply different annual cycles. Perhaps the most comprehensive discussion of the seasonal variation of the GEC so far has been given by Adlerman and Williams (1996). We will review the findings of this paper, together with other results in this direction, in Section 2 below. Among other things, we shall revisit the seasonal cycle obtained by Burns et al. (2012) on the basis of PG measurements at Vostok during 1998–2001 and various seasonal patterns derived from air—Earth current measurements.

The fact that different data sets do not agree with each other in predicting the seasonal variation of the GEC already implies that the real effect may be subtle and difficult to discern in measurements owing to the dominance of annual cycles of local factors. This suggests that in order to find the actual globally representative variation, one needs a large consistent data set obtained in a clean location with a small influence of local effects. For this study we shall use the results of PG measurements at Vostok during 2006–2020; this data set is much longer than data sets from the same location discussed in the literature before. It is also very important that the Vostok data have been recorded continuously, which makes it possible to precisely calculate diurnal mean values (we will demonstrate that it is very important when one discusses the seasonal variation of the GEC). A more detailed description of the data will be given in Section 3.

The Vostok PG data have already proved to be very useful in studying other modes of atmospheric variability, clearly demonstrating certain variation patterns related to the El Niño—Southern Oscillation (Slyunyaev, Frank-Kamenetsky, et al., 2021) and the Madden–Julian oscillation (Kozlov et al., 2023). At the same time earlier discussions of the seasonal variation of the GEC employed only relatively little Vostok PG data partially covering 1998–2004 and 2006–2011 (e.g., Burns et al., 2012; Lavigne et al., 2017). In Section 4 of this article we will present new results following from the longer Vostok PG time series covering 2006–2020 (with only one major gap in the data during the second half of 2017). We shall also demonstrate that these results can be interpreted in terms of the variation of insolation, providing further evidence in support of the link between the GEC and insolation earlier discussed by Williams (1994) and Adlerman and Williams (1996). Finally, in Section 5 the patterns of variation known from the literature will be revisited in the context of new findings.

This article (Part 1) comprises the first part of a study of the seasonal variation of the GEC; its main focus will be on measurements (including both a critical discussion of earlier results published in the literature and a new analysis on the basis of the long-term Vostok PG data set). In Part 2 (which will be published as a separate article) we shall further investigate the same problem using IP simulations in weather and climate models.

2. Earlier Studies of the Seasonal Variation of the GEC

The analysis and interpretation of annual variation patterns inferred from various atmospheric electricity measurements have a very long and complicated history. A thoughtful review of this history, together with further analysis, can be found in the paper by Adlerman and Williams (1996), and here we shall restrict ourselves to summarizing the main findings from the present-day perspective.

2.1. Main Parameters of the GEC

We begin by reviewing the main parameters characterizing the GEC and the equations linking these parameters. Let z be the altitude above sea level. We suppose that one can partition the entire atmosphere into a number of one-dimensional vertical columns (horizontal cross-sections of these columns may have arbitrary shapes) such that the distributions of the air conductivity and vertical source current density in the nth column are approximated by functions $\sigma_n(z)$ and $j_n^{\mathrm{s}}(z)$, respectively (the source current represents charge separation inside electrified clouds, whence $j_n^{\mathrm{s}}(z) = 0$ outside such clouds).

In each column we consider the problem in a one-dimensional approximation. If $\phi_n(z)$ and j_n are the electric potential and vertical electric current density in the nth column, then it follows from Ohm's law that

$$j_n = -\sigma_n(z) \frac{d\phi_n}{dz}(z) + j_n^{\mathrm{s}}(z); \tag{1}$$

note that j_n does not depend on z in our one-dimensional approximation owing to the current continuity equation (we assume that the current inside each column is purely vertical). The condition establishing the balance of the electric current on the Earth's surface reads as

$$\sum_n j_n S_n = 0, \tag{2}$$

where S_n is the area covered by the nth column. Note that in practice $j_n < 0$ for fair-weather columns (where $j_n^s(z) = 0$ for all z) and $j_n > 0$ for columns occupied by electrified clouds (where there is a range of altitudes with $j_n^s(z) > 0$).

Let $h_{\max}$ be the height of the outer boundary of our model of the atmosphere, which we assume to be nearly equipotential (in practical computations $h_{\max}$ can be set equal to about 70 km). If we denote the IP by V, then in view of Equation 1 we shall have for any column

$$V = \int_0^{h_{\max}} \frac{d\phi_n}{dz}(z)\, dz = \int_0^{h_{\max}} \frac{j_n^s(z)\, dz}{\sigma_n(z)} - j_n \int_0^{h_{\max}} \frac{dz}{\sigma_n(z)}, \tag{3}$$

which, together with Equation 2, after a simple calculation yields a formula representing the IP in terms of $\sigma_n(z)$ and $j_n^s(z)$:

$$V = \sum_n S_n \int_0^{h_{\max}} \frac{j_n^s(z)\, dz}{\sigma_n(z)} \left(\int_0^{h_{\max}} \frac{dz}{\sigma_n(z)} \right)^{-1} \Bigg/ \sum_n S_n \left(\int_0^{h_{\max}} \frac{dz}{\sigma_n(z)} \right)^{-1}. \tag{4}$$

We have already noted that the IP is probably the most fundamental characteristic of the GEC intensity. Equation 4 indicates that it is determined by global distributions of the conductivity and source current density and should not be very sensitive to local perturbations. The situation is different for other parameters important for atmospheric electricity measurements, namely the PG and air—Earth current density in fair-weather regions.

If the nth column in our representation of the atmosphere is characterized by fair weather, we obviously have $j_n^s(z) = 0$, whence, by virtue of Equations 1 and 3,

$$|j_n| = V \left(\int_0^{h_{\max}} \frac{dz}{\sigma_n(z)} \right)^{-1} \tag{5}$$

and

$$\frac{d\phi_n}{dz}(0) = \frac{|j_n|}{\sigma_n(0)} = \frac{V}{\sigma_n(0)} \left(\int_0^{h_{\max}} \frac{dz}{\sigma_n(z)} \right)^{-1}. \tag{6}$$

Equations 5 and 6 describe the fair-weather air—Earth current density and PG at the Earth's surface, respectively. It is easy to see that these quantities do not simply reflect the variation of the IP V, being additionally influenced by local conductivity changes. While the air—Earth current depends only on the total resistance of the entire air column, which may not be so sensitive to local conductivity perturbations, the surface PG is also directly linked to the value of the conductivity at the observation point. According to Equations 5 and 6, global conductivity changes may also lead to different patterns of variation for the IP, the air—Earth current density, and the surface PG. However, in this paper we shall not consider such subtle effects; we shall suppose that in the absence of local perturbations all of the three aforementioned parameters vary in agreement with each other, which justifies our occasional use of the universal expression “GEC intensity.”

Note that we derived Equations 5 and 6 assuming that there are no source currents in fair-weather regions. If we took into account the so-called Austausch generator, related to a vertical transport of space charge due to turbulent convection in the boundary layer (e.g., Kasemir, 1956; Mareeva et al., 2011; Willett, 1979), this would produce additional source currents near the Earth's surface in fair-weather regions, and we would not be able to drop the first term in the right-hand side of Equation 3 anymore. The extent of validity of the classical Ohm's law without source currents in the context of surface atmospheric electricity measurements has been discussed and analyzed before, for example, by Dolezalek (1960a, 1960b) and Bhartendu (1971b).

To summarize the above, among the parameters of the GEC that can be measured directly, the IP immediately represents the global signal, the fair-weather air—Earth current density may be influenced by local conductivity changes to some extent, and the fair-weather PG at the Earth's surface is essentially affected by such perturbations. In the following sections we will review the results concerning the seasonal variation of the GEC inferred from measurements of all these parameters.

2.2. Measurements of the Fair-Weather PG

The fair-weather PG at the Earth's surface is probably the easiest atmospheric electrical parameter to measure on a regular basis. Already in 1860 Lord Kelvin observed that the fair-weather electric field in Europe is much greater in winter than in summer (see Thomson, 1860, later reprinted in Thomson, 1884). By the beginning of the twentieth century, atmospheric electricity observations had established a firm belief of a clear wintertime maximum for the fair-weather PG in the Northern Hemisphere (e.g., Exner, 1900). At the same time it turned out that in the Southern Hemisphere the PG behaves oppositely, reaching maximum values during the boreal summer (e.g., Halliday, 1933), which coincides with the austral winter, and in the tropics the seasonal variation of the PG is unclear (see Adlerman & Williams, 1996, Figure 1).

This reversal in the seasonal behavior between the two hemispheres suggests a strong influence of local effects, and already in the first half of the twentieth century it was known that atmospheric electricity measurements are substantially affected by atmospheric pollution (Builder, 1929; Chree & Watson, 1924; Halliday, 1933; Wait, 1927; Whipple, 1929b). A comprehensive analysis of this issue from a modern viewpoint was carried out by Adlerman and Williams (1996), who demonstrated that much higher aerosol concentrations over the continents during local winters lead to lower conductivity values and, by inference, to greater PG values (see our Equation 6 above). In particular, Adlerman and Williams (1996) emphasized the role of Aitken condensation nuclei (aerosol particles less than 1 μm in diameter), whose annual variation may be linked to seasonal changes in atmospheric dispersion characteristics, as well as production rates of man-made aerosols and wind-generated soil aerosols.

Thus continental PG measurements cannot answer the question as to where the true annual maximum of the GEC intensity occurs, inasmuch as its seasonal variation is obscured by pronounced seasonal cycles of local aerosol concentrations and conductivity. It is known that PG values obtained at different land stations often show a poor correlation between each other (Bhartendu, 1971a). In this connection the results of measurements at clean locations (i.e., those with a small aerosol variability) become especially important.

Perhaps the most famous data of this kind are the PG values obtained on board the Carnegie research vessel during several cruises in 1915–1921 and 1928–1929 (Ault & Mauchly, 1926; Torreson et al., 1946). For many decades it was widely thought that the Carnegie data imply a wintertime maximum in the GEC intensity, after such a conclusion had been inferred in the analysis of Parkinson and Torreson (1931). However, as pointed out by Adlerman and Williams (1996), this inference was based on a very limited sampling involving the data from only one cruise of the Carnegie ship (in particular, only 7 days were considered from the months of May, June and July).

Adlerman and Williams (1996) reexamined the Carnegie measurements and analyzed them more thoroughly. To this end they produced a much larger data set by combining together the PG data from different Carnegie cruises and supplementing them with the results of PG measurements on board the Maud ship in 1922–1925 (Sverdrup, 1926). This data set has revealed that the PG values collected during Carnegie and Maud expeditions actually imply the highest GEC intensity during the Northern Hemisphere summer (rather than the winter). The corresponding variation with a peak in July, obtained by Adlerman and Williams (1996), is shown in Figure 1a; here fair-weather values were determined by demanding that the PG be smaller than 300 V/m. The peak-to-peak amplitude of this variation is equal to about 53% of the annual mean value (when the original data are not available to us, we estimate the annual mean by averaging 12 monthly mean values); a major portion of this amplitude is due to the pronounced maximum in June–July.

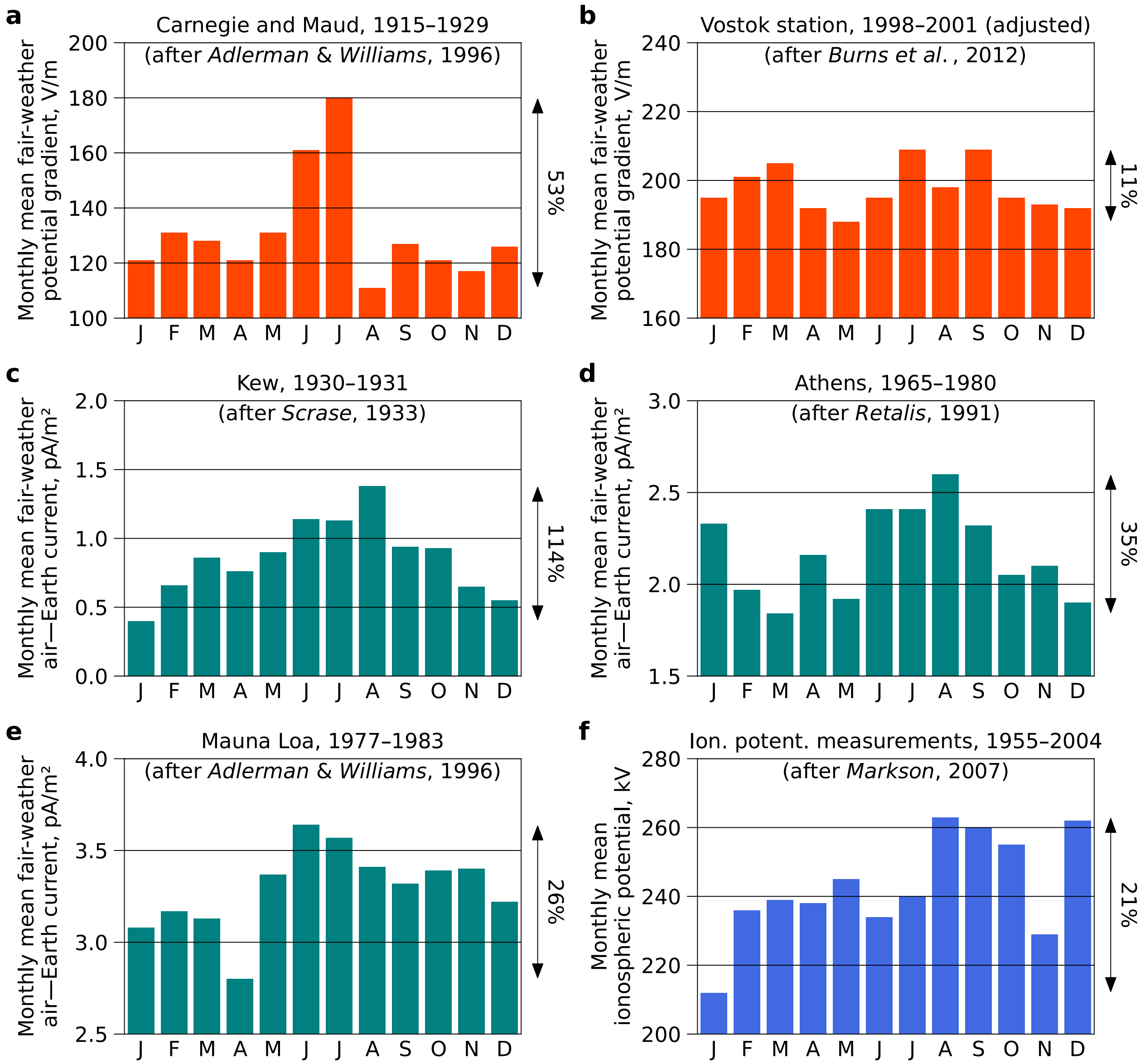

Figure 1. (a, b) Monthly mean values of the fair-weather PG according to measurements on board the Carnegie and Maud research vessels in 1915–1929 (a; after Adlerman & Williams, 1996, Figure 7b) and at the Vostok station in 1998–2001 (b; after Burns et al., 2012, Table 2 and Figure 13; the data adjusted for local meteorological and solar wind influences). (c–e) Monthly mean values of the fair-weather air—Earth current according to measurements at Kew Observatory, London, UK, in 1930–1931 (c; after Scrase, 1933, Table 2), at the National Observatory of Athens, Greece, in 1965–1980 (d; after Retalis, 1991, Figure 6), and at Mauna Loa, Hawaii, USA, in 1977–1983 by W. E. Cobb (e; after Adlerman & Williams, 1996, Figure 6). (f) Monthly mean values of the IP according to measurements by J. F. Clark, R. Mühleisen and H. J. Fischer, and R. Markson during 1955–2004 (after Markson, 2007, Figure 7). See the main text for further details. The double arrow to the right of each panel represents the peak-to-peak amplitude, and the number next to it gives this amplitude as a fraction of the annual mean (estimated based on monthly values).

Note, however, that the interpretation of seasonality in the Carnegie and Maud data appears to be a subtle issue, for the results may significantly depend on the criteria used to select fair-weather values. The variation shown in Figure 1a is based on the PG values smaller than 300 V/m; using lower thresholds substantially reduces the peak-to-peak amplitude of the variation, although the summer peak in July still remains (see Adlerman & Williams, 1996, Figure 7a). There are also reports that summertime values of the fair-weather PG measured on board the Carnegie are actually lower than wintertime values even if one considers the data from multiple cruises (see Harrison & Nicoll, 2008, Figure 8e), which apparently contradicts the variation shown in Figure 1a. A possible reason behind this contradiction is that the original Carnegie data do not form a consistent hourly time series (see Ault & Mauchly, 1926; Torreson et al., 1946), and the patterns inferred from them may crucially depend on the details of data selection criteria and averaging procedures. This already demonstrates the difficulty of determining the seasonal variation from observed PG values even at clean locations.

Measurements over the ocean are not the only option when it comes to reducing the influence of aerosols on the fair-weather PG at the Earth's surface. It is equally interesting to look at the data collected at remote Antarctic stations, especially those located on the high Antarctic plateau. Figure 1b shows the seasonal variation of the fair-weather PG obtained by Burns et al. (2012) from measurements at the Vostok station during 1998–2001; certain corrections for the variability of local meteorological factors and for the solar wind influence were applied when calculating the PG values. This variation is much less pronounced than that based on the Carnegie and Maud data (see Figure 1a), having only an 11% peak-to-peak amplitude (relative to the annual mean); at the same time it also has a maximum in July (note, however, that there is another maximum of the same magnitude in September and a somewhat smaller maximum in March). Later in this paper we shall analyze a much larger data set containing PG values from Vostok (covering almost the entire period of 2006–2020).

2.3. Measurements of the Fair-Weather Air—Earth Current Density

The main problem with finding global signals in the results of PG measurements is related to local conductivity perturbations in the boundary layer. To reduce the influence of this factor, it is reasonable to consider the air—Earth current density, which, according to Equations 5 and 6, should be more representative of global trends in the GEC than the PG.

One of the first attempts to infer the seasonal behavior of the GEC from continual air—Earth current measurements was made by Scrase (1933) on the basis of measurements at Kew Observatory (London, UK) over one year from June 1930 to May 1931. The resulting variation, later reproduced by Chalmers (1967) in his book on atmospheric electricity, is shown in Figure 1c; here we see a very pronounced seasonal change with a maximum during the Northern Hemisphere summer (the highest value is reached in August). Here the difference between the maximum and the minimum actually exceeds the annual mean value, which casts doubt on the reliability of these measurements: We will see below that no other data set comes close to this one in terms of the estimated peak-to-peak amplitude.

An analysis of a much longer time series of measurements at Kew Observatory (spanning seven decades from 1909 until 1979) in the context of the seasonal variation of the GEC was done by Harrison and Ingram (2005). They plotted seasonal variations of the air—Earth current measured around 15 UTC separately for 1909–1931, 1932–1949, and 1967–1979 (the 1950s and early 1960s were neglected owing to atmospheric electricity parameters being affected by nuclear weapons testing; see, e.g., Markson, 2007). The plots for 1909–1931 and 1932–1949 show two maxima near the equinoxes (the main maximum in August–September and a slightly less pronounced secondary peak in April), while the data for 1967–1979 yielded a less clear pattern with the principal maximum in October (see Harrison & Ingram, 2005, Figure 3). Note, however, that this longer time series contains only the results of measurements made on fine afternoons around 15 UTC, whereas the analysis of Scrase (1933) was based on an hourly time series and true diurnal mean values. This further complicates the interpretation of the findings inferred from the long Kew data set, as it is well known that the shape of the diurnal cycle of the GEC undergoes a substantial seasonal change (see, e.g., Burns et al., 2017), which means that the annual variation in the GEC intensity at specific hours of the day may differ from its counterpart derived from diurnal mean values (we will demonstrate this more clearly in Section 4.2 below).

Hogg (1950) compiled the results of air—Earth current measurements from 17 stations at various locations all over the globe. For the majority of these stations, the seasonal variation appears to have a pronounced semiannual component (with two maxima around spring and autumn; see Hogg, 1950, Table 4). However, most of these data sets correspond to measurements at specific UTC hours and only a few are based on continuous measurements. Moreover, as pointed out by Adlerman and Williams (1996), at all except three of these stations the current had been measured by an indirect method (i.e., by multiplying the PG by the conductivity), which may be less precise in determining the conduction current. Indeed, apart from the greater error introduced by such an approach, in practice the classical Ohm's law (asserting that the product of the PG and the conductivity is equal to the total current density) may not be fulfilled (Bhartendu, 1971b), in which case the calculated product would be less representative of global patterns and trends (note, however, that the total current itself in this case would be slightly different from that described by Equation 5 and, by inference, also less globally representative). All this makes it difficult to infer clear conclusions about the mean seasonal variation of the GEC from the data presented by Hogg (1950); for a more detailed discussion, see Williams (1994) and Adlerman and Williams (1996).

Retalis (1991) analyzed the results of air—Earth current density measurements made at the National Observatory of Athens (Athens, Greece) during 1965–1980. In Figure 1d we reproduce the seasonal variation cycle for fair weather which he obtained based on these data. Similarly to the hourly Kew data, the air—Earth current at Athens reaches highest values in the Northern Hemisphere summer, with the main maximum in August. During the Northern Hemisphere winter the current is generally low, except that the January value is unusually large; there are also several less pronounced local maxima. The peak-to-peak amplitude of the variation is about 35% of the mean.

Another data set containing hourly values of the air—Earth current density was obtained by W. E. Cobb at the Mauna Loa Observatory (Hawaii, USA). Adlerman and Williams (1996) analyzed Cobb's data for 1977–1983 (with some gaps in 1978) and plotted the corresponding seasonal variation, which is reproduced here in Figure 1e. Similarly to the hourly Kew data and the Athens data, the current at Mauna Loa is largest in the boreal summer, but the maximum value is attained in June. Adlerman and Williams (1996) pointed out the anomalously low April value, which they associated with the transport of desert dust from Asia. The peak-to-peak amplitude of about 26% (relative to the annual mean) is to a large extent determined by this April minimum.

One more hourly time series for the air–Earth current was obtained at Lerwick Observatory (Shetland Islands, UK) in 1978–1984. The values corresponding to 15 UTC in these data were later analyzed by Harrison and Nicoll (2008). They arrived at a seasonal variation for which the main maximum occurs in January with additional peaks in October and April, that is, near the equinoxes (see Harrison & Nicoll, 2008, Figure 9b). As with the long time series of measurements at Kew described above, it is difficult to compare this variation with those from other sites in view of the fact that seasonal behavior for diurnal mean values and values at 15 UTC is likely to be different.

A few other air—Earth current density data sets (none of which yields clear inferences about the behavior of the GEC on the annual timescale) will be mentioned in Section 5.4 below, where we shall revisit the data described above in the context of our own findings.

2.4. Measurements of the IP

In contrast to the fair-weather PG and air—Earth current, the IP directly represents the GEC intensity and should not be affected by any local conductivity changes. At the same time its measurement requires rather expensive aircraft or balloon soundings, for which reason there are little IP data available, and the identification of actual variations is usually difficult owing to insufficient sampling.

The first attempt to infer the seasonality of the GEC from measured IP values was made by Fischer (1962; the figure was later reproduced by Chalmers, 1967, Figure 53). He arrived at a wintertime maximum, although, as noted by Markson (2007), this may be a consequence of the fact that his data included only a few measurements during the Northern Hemisphere summer. More recently, Markson (2007) compiled together and analyzed the results of IP soundings obtained by different researchers (J. F. Clark, R. Mühleisen and H. J. Fischer, and R. Markson himself) over 1955–2004. The seasonal cycle which he obtained on the basis of the diurnally normalized (according to the Carnegie curve) IP data set is shown in Figure 1f. This variation has a maximum in August; another maximum in December, according to Markson (2007), is not reliable, being based on only six measurements obtained during the nuclear weapons testing period. More generally, Markson (2007) noted that all the values for November through January are less reliable owing to the relatively small number of observations during these months (hence the estimated peak-to-peak amplitude of 21% is also insufficiently reliable). In addition, it is difficult to infer true diurnal mean IP values from a data set containing results of measurements at different UTC hours: Owing to the prominent seasonal change of the diurnal cycle of the GEC, any simple correction for the diurnal variation, strictly speaking, will be insufficient.

2.5. Summary of Observations

Comparing once again different panels of Figure 1 and taking into account the results of other studies mentioned above, we conclude that it is very difficult to determine the seasonal variation of the GEC from measurements of atmospheric electricity parameters. The main difficulties include the small amount of available data and insufficient sampling in the case of the IP, a strong impact of local conductivity changes in the case of the PG (and, to a lesser extent, in the case of the air—Earth current as well), the apparent dependence of the seasonal behavior of the GEC intensity on the UTC hour (which hinders comparing some data sets with each other), not to mention possible errors and uncertainties related to measurement procedures and data selection. Also, to reliably determine the average seasonal variation of the GEC from measurements, one probably needs the data covering at least several years so as to eliminate the effect of other modes of atmospheric variability, mainly of the El Niño—Southern Oscillation (e.g., Harrison et al., 2022; Slyunyaev, Ilin, et al., 2021).

In view of all this, it is hard to be certain about the real seasonal variation pattern in the GEC intensity. The variations shown in Figure 1 generally indicate the highest magnitude of GEC parameters during the Northern Hemisphere summer; at the same time the amplitude of the variation and the positions of other maxima and minima vary for different data sets. Apart from that, we have already mentioned that there are some studies where even the main maximum occurs during a different season (note, however, that at least part of these studies are based on GEC parameters at specific UTC hours, which implies that such results do not necessarily contradict Figure 1). Let us recall that in this article we focus on the DC GEC; it is known that the seasonal variation of global lightning activity and of the intensity of Schumann resonances, excited by lightning in the Earth—ionosphere cavity (which form the AC GEC), has a substantially greater amplitude and exhibits a clear maximum during the boreal summer (e.g., Christian et al., 2003; Hayakawa et al., 2023; Price & Melnikov, 2004). However, for the DC GEC, maintained by both thunderstorms and ESCs, seasonal changes appear to be notably less pronounced (the same is true on the diurnal timescale; see, e.g., Mach et al., 2011; Williams & Heckman, 1993). We will revisit the variation plots shown in Figure 1 in Section 5, where they will be given a more detailed discussion in view of our own findings.

3. Methods and Data

In this section we describe the data which we shall use below for further analysis of the seasonal changes in the GEC. These data include (a) the results of PG measurements at the Vostok station in Antarctica and (b) surface air temperature values simulated using the weather forecasting model WRF (Weather Research and Forecasting model) on the basis of meteorological reanalysis data.

3.1. Processing the Results of PG Measurements at the Vostok Station

We have already mentioned that the results of PG measurements in Antarctica, and especially those obtained at the high Antarctic Plateau far from the coast, are generally considered less affected by local conductivity perturbations than PG data collected in most locations on other continents. The air over the surface of the Antarctic Plateau is almost entirely free of radon, as well as of sea salt and man-made aerosols; in addition, during the most part of the year the boundary layer is stable, preventing vertical air motions (e.g., Burns et al., 2017). In this study we will analyze seasonal changes inferred from the results of continual PG measurements at the Vostok station during 2006–2020.

During these years, the PG was regularly measured at Vostok using a rotating-dipole field mill, which had been installed there at the end of 2005 (Burns et al., 2017; note that the Vostok data for 1998–2001, which yielded the seasonal variation shown in Figure 1b, had been obtained with a different field mill). The results of PG measurements were collected in the form of mean values over consecutive 10-s periods; however, owing to technical reasons only 5-min mean values are available for some periods of time, including the entire year 2017.

First of all, we transformed all the available PG data into average values over consecutive hours. Sometimes there are gaps in the data; for this reason, when averaging, we retained only those hours for which at least 80% of the PG values are known (cf. Burns et al., 2005). Also, in order to remove the disturbance caused by the metal pole which supported the field mill, all measured PG values were divided by a form factor gradually changing from 3 at the beginning of 2005 to about 2.5 at the end of 2020; this gradual decrease of the form factor is due to the constant accumulation of wind-drifted snow around the metal pole (for more details, see Supporting Information S1).

Next, we identified and selected fair-weather days. The same formal procedure was applied which had been earlier used by Slyunyaev, Frank-Kamenetsky, et al. (2021) and Kozlov et al. (2023): We (a) removed the days with incomplete or absent hourly data, (b) removed the days with negative or zero hourly PG values, (c) removed the days with hourly PG values exceeding 300 V/m, and (d) among the remaining days retained only those for which the diurnal peak-to-peak amplitude does not exceed 150% of the diurnal mean.

3.2. Simulating Surface Air Temperature With the WRF Model

Our discussion of the seasonal variation will also require knowing the distribution of surface air temperature over the Earth's surface. For this study we used air temperature values at 2 m above the ground obtained with the help of the weather forecasting model WRF (e.g., Powers et al., 2017; Skamarock et al., 2019), which had been run globally on a $1° \times 1°$ latitude-longitude grid to simulate the atmospheric dynamics during 1980–2020, with ERA5 (fifth generation European Center for Medium-Range Weather Forecasts reanalysis) meteorological reanalysis data (Hersbach et al., 2023) used as initial conditions in model runs. Technical details of the WRF simulations are described in Supporting Information S1; in Part 2 of this study the same model runs will be used to simulate contributions to the IP.

3.3. Estimating the Solar Wind Imposed Potential Difference Over Vostok

To estimate the effect of the solar wind on Vostok PG values, we will need to know the variation of the solar wind imposed potential difference above the station. Such potential differences over the polar caps are commonly evaluated using empirical models based on interplanetary magnetic field and solar wind parameters. For this study we employed the Weimer 2005 model (Weimer, 2005a, 2005b, 2019) and the near-Earth solar wind magnetic field and plasma parameters taken from NASA (National Aeronautics and Space Administration) Goddard Space Flight Center (GSFC) Space Physics Data Facility's OMNI data set (King & Papitashvili, 2005; Papitashvili & King, 2020). Technical details of these calculations are given in Supporting Information S1.

4. New Results and Their Analysis

Now we will further investigate the seasonal variation of the GEC using the data set described in Section 3.1 (the PG measured at the Vostok station during 2006–2020).

4.1. The Seasonal Behavior Inferred From the New Vostok Data

Figure 2a shows the average seasonal behavior of the fair-weather PG values obtained at Vostok during 2006–2020. Here we observe a variation with lowest values attained in January–February and highest values reached in June–August; more precisely, there are two close maxima in June and August with a small local minimum in July between them. Thus the PG variation at Vostok has a pronounced annual component with a maximum and minimum during the Northern Hemisphere summer and winter, respectively. The peak-to-peak amplitude of this variation is about 30% of the mean, which is substantially larger than the value inferred from the analysis of the 1998–2001 Vostok data by Burns et al. (2012), reproduced in Figure 1b. The pattern of variation is also quite different: In 2006–2020 we do not see low PG values around May, which have been reported by Burns et al. (2012) for the earlier data. We will return to the discussion of different data sets from Vostok in Sections 5.2 and 5.3.

Let us now investigate whether the behavior described above is stable and reproducible. Dividing the whole 2006–2020 period, used to plot Figure 2a, into two smaller periods (2006–2012 and 2013–2020), we show the corresponding “partial” seasonal cycles in Figures 2b and 2c (annotations inside the bars in these two panels as well as in Figure 2a indicate the number of fair-weather days used to calculate the respective monthly values). We observe that the two “partial” variation patterns are very similar to each other, having a prominent maximum during the Northern Hemisphere summer (with the highest value in August) and a minimum during the Northern Hemisphere winter (with the lowest value in January). The annual mean PG value for 2013–2020 is somewhat smaller than its counterpart for 2006–2012, but the peak-to-peak amplitude of the annual variation (relative to the mean) for these time spans turns out to be nearly identical. It is also remarkable that both “partial” cycles independently predict a small local minimum in July amid the flat summer maximum; we will discuss this observation in Section 4.3 below.

Thus we can state that the shape of the seasonal variation in the GEC intensity at Vostok is independently reproduced for two different sufficiently long time periods, even though these periods are characterized by different mean PG values. This gives us hope that there probably exists a universal average annual cycle of the

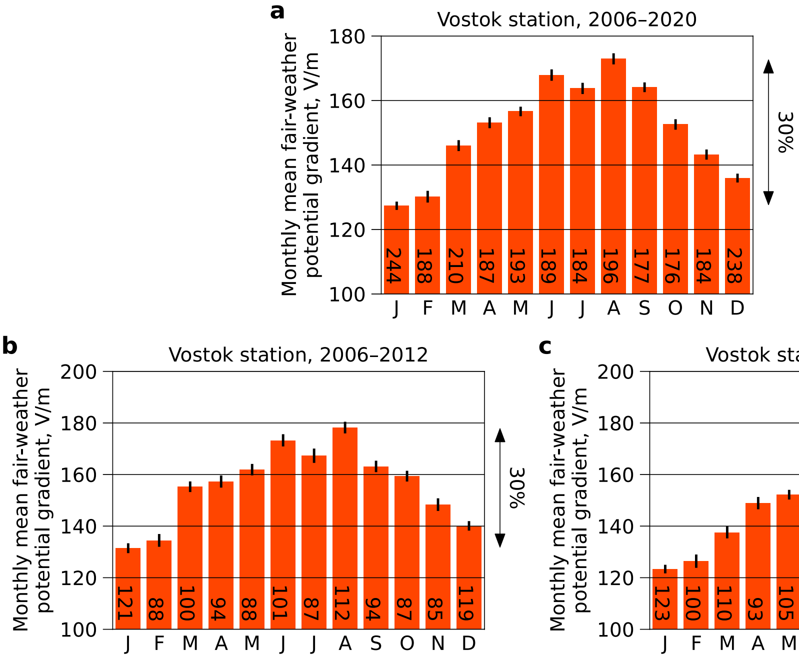

Figure 2. (a) Monthly mean values of the fair-weather PG according to measurements at the Vostok station in 2006–2020. (b, c) Monthly mean values of the fair-weather PG according to measurements at the Vostok station for two different time periods (2006–2012 and 2013–2020) within the 2006–2020 data set used to plot panel (a). Annotations inside the bars in all panels indicate the number of fair-weather days used to calculate the average values. Error bars demonstrate the values plus and minus one standard error. The double arrow to the right of each panel represents the peak-to-peak amplitude, and the number next to it gives this amplitude as a fraction of the annual mean.

GEC (in a sense, similar to the Carnegie curve on the diurnal timescale). Note that the pattern of variation shown in Figure 2 represents the average seasonal cycle at Vostok and may not be observed when one considers individual years separately (to illustrate this, monthly mean PG values for 15 individual years within 2006–2020 are shown in Figure S1 in Supporting Information S1); moreover, even averaging over two or three consecutive years is usually not enough (see Figure S2 in Supporting Information S1). This situation is also similar to the usual behavior of the GEC on the diurnal timescale: On individual days one generally observes somewhat different patterns of variation, while taking the average over many such days yields the universal Carnegie curve.

4.2. Seasonal Variation as a Function of the UTC Hour

Until this moment we have been studying the seasonal variation of the diurnal mean GEC intensity (i.e., we considered the diurnal mean PG on fine days). In the literature, however, one can also find studies of the seasonal variation of the GEC on the basis of the values of atmospheric electrical parameters at specific UTC hours (e.g., Harrison & Ingram, 2005; Harrison & Nicoll, 2008) or even on the basis of a compilation of values obtained at different hours (with a certain correction; see, e.g., Markson, 2007). In Section 2 we have already mentioned several times that the shape of the diurnal cycle of the GEC undergoes a substantial seasonal change (Burns et al., 2017), which implies that, generally speaking, seasonal behavior of GEC parameters at specific UTC hours may be substantially different from the behavior of the respective diurnal mean values.

In this section we shall investigate this situation in more detail, looking at the GEC variation on the diurnal and seasonal timescales simultaneously. To plot both variations at the same time, we will use a diurnal-seasonal diagram in which the horizontal axis represents the UTC hour, the vertical axis represents the month, and different magnitudes of the fair-weather PG are indicated by different colors (cf. Lavigne et al., 2017; see also a similar diagram for the IP in Fischer, 1962). Figure 3a demonstrates such a diagram for the fair-weather PG at Vostok (based on all measurements performed during 2006–2020). Clearly vertical cross-sections of this diagram represent the seasonal variation of the PG at different UTC hours, while its horizontal cross-sections yield its diurnal variation in different months. The corresponding seasonal variation of the diurnal mean PG is shown here in a separate column to the right of the main diagram; this is just another representation of the bar plot shown in

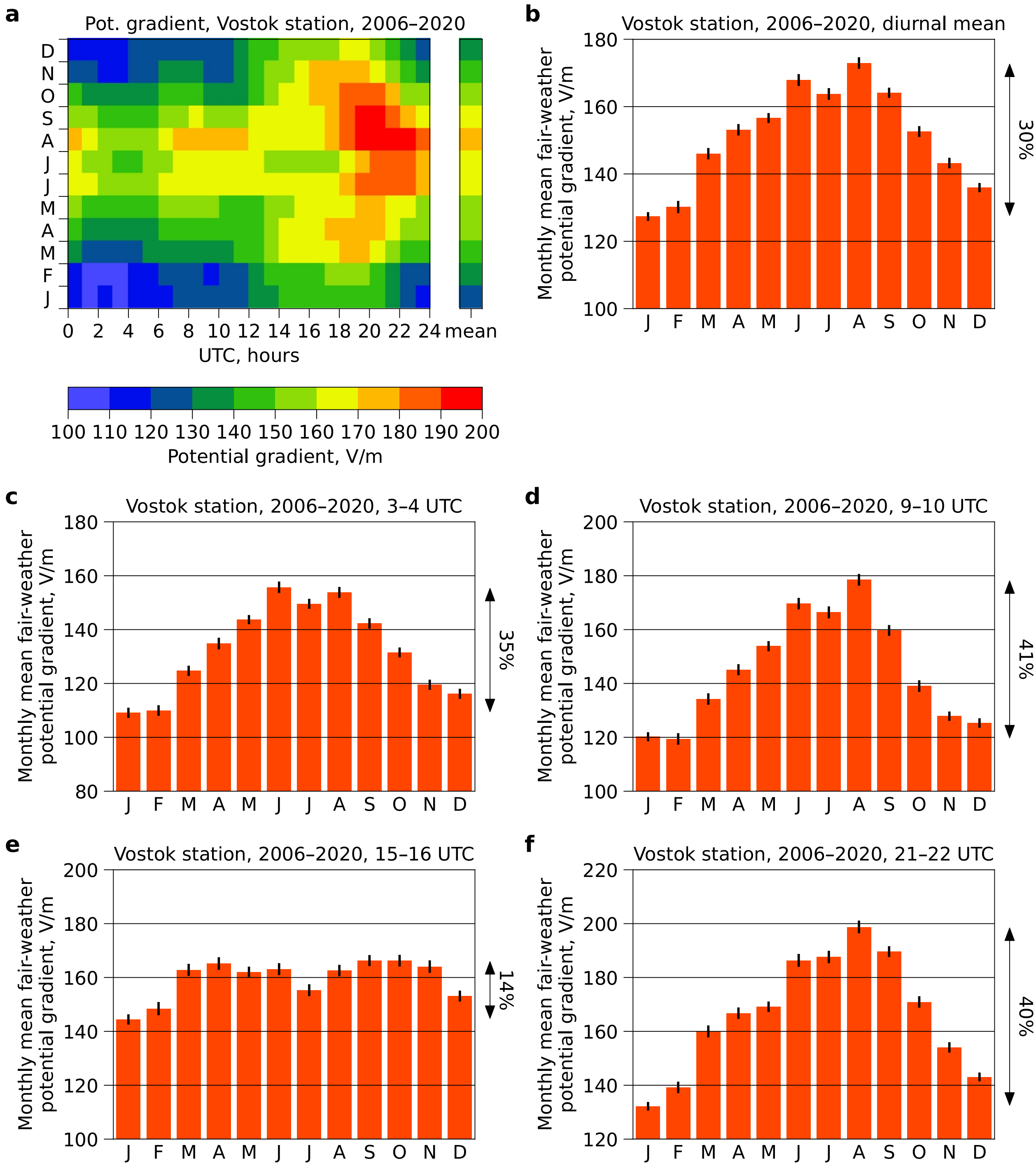

Figure 3. (a) Diurnal and seasonal distribution of the fair-weather PG values measured at the Vostok station during 2006–2020. The column to the right of the main diagram shows the seasonal variation of the diurnal mean value; this variation is shown as a bar chart in panel (b). (b) Monthly mean values of the fair-weather PG according to measurements at the Vostok station in 2006–2020 (the same as Figure 2a). (c–f) Monthly mean values of the fair-weather PG at specific UTC hours, namely 3–4 UTC (c), 9–10 UTC (d), 15–16 UTC (e), and 21–22 UTC (f), according to measurements at the Vostok station in 2006–2020. Error bars in all panels demonstrate the values plus and minus one standard error. The double arrow to the right of each panel represents the peak-to-peak amplitude, and the number next to it gives this amplitude as a fraction of the annual mean value.

Figure 2a, which for convenience is reproduced here as Figure 3b. A similar diurnal-seasonal diagram on the basis of combined Vostok PG data for 1998–2004 and 2007–2011 was earlier plotted by Lavigne et al. (2017, Figure 1a). Our Figure 3a generally agrees with it, as we might have expected seeing that our data set for 2006–2020 overlaps with that used by Lavigne et al. (2017).

Looking at Figure 3a and comparing vertical cross-sections of the diagram at different UTC hours with the corresponding diurnal mean variation, shown on the right, we observe that values of the fair-weather PG at individual UTC hours are not necessarily representative of the average behavior, as we have expected. Seasonal cycles at individual UTC hours generally agree with the average behavior in reaching highest values during the Northern Hemisphere summer, but the shape of the variation gradually changes during the day. It is interesting that the small local minimum of the PG in July, which we earlier pointed out in all three panels of Figure 2, is clearly seen in the diurnal-seasonal diagram during 1–7 UTC and 13–18 UTC; at other hours of the day this minimum may also be present but the diagram does not necessarily resolve small local fluctuations owing to the limited number of colors that we employ.

Figures 3c–3f show monthly mean values of the fair-weather PG at Vostok corresponding to four specific UTC hours, namely 3–4 UTC, 9–10 UTC, 15–16 UTC, and 21–22 UTC; in other words, these bar plots visualize four vertical cross-sections of the diurnal-seasonal diagram of Figure 3a. We immediately observe that although all these variations are somewhat similar to the diurnal mean variation, shown in Figure 3b (e.g., all of them agree in showing lowest PG values during the Northern Hemisphere winter), their magnitudes are essentially different (from 14% in the case of 15–16 UTC to 41% in the case of 9–10 UTC). Moreover, Figures 3c–3f demonstrate that the shapes of the variations at specific hours are also notably different and not necessarily representative of the variation for the diurnal mean value: While the bar plots for 3–4 UTC, 9–10 UTC, and 21–22 UTC generally resemble the average behavior, reaching highest values during the Northern Hemisphere summer, the annual cycle at 15–16 UTC has two distinct maxima in spring and autumn, thus emphasizing the semiannual component of the variation. One can speculate that this behavior may be due to the highest contribution of Africa to the GEC at these hours of the day, for it is known that lightning activity over Africa (which must be to some extent correlated with the local contribution to the GEC) exhibits a semiannual signal (e.g., Blakeslee et al., 2014; Williams & Sátori, 2004). It is interesting that the seasonal cycles based on air—Earth current density measurements around 15 UTC at Kew (Harrison & Ingram, 2005, Figure 3) and Lerwick (Harrison & Nicoll, 2008, Figure 9b) also demonstrate a pronounced semi-annual component with maxima around the equinoxes. These observations once again clearly demonstrate that one should be very careful when comparing the seasonal cycles based on the data collected at different UTC hours.

4.3. Interpretation of the Observed Seasonal Behavior

When Adlerman and Williams (1996) discussed the seasonal cycle of the GEC, they linked seasonal changes in deep convection (which is correlated with the occurrence of electrified clouds) to the variability of insolation. In the tropics the annual variation of insolation has two maxima around the equinoxes, while outside the tropics it has a single pronounced maximum during the local summer. Williams (1994) pointed out that surface air temperature generally follows the variation of insolation with a lag of about 1 month and thus is also correlated with atmospheric electrical parameters. Following these ideas, we shall now consider the behavior of surface air temperature in order to provide a physical interpretation for the pattern of variation shown in the three panels of Figure 2. To this end we will use air temperature values at 2 m above the ground derived from the results of WRF simulations for 1980–2020 (see Section 3.2).

The four panels of Figure 4 show monthly mean values of the surface air temperature averaged over different symmetric latitude ranges around the equator. In the region lying between 20°S and 20°N (Figure 4a) the mean temperature has two maxima following the equinoxes. When we turn to broader regions of 30°S–30°N (Figure 4b) and 40° S–40° N (Figure 4c), the two maxima become closer to each other, and in Figure 4c they are separated only by a small local minimum in July. Finally, the mean surface air temperature for 50°S–50°N (Figure 4d) has only one maximum in August, that is, during the Northern Hemisphere summer.

The results presented in our Figure 4 generally agree with the mean temperature variations for 25°S–25°N and 60°S–60°N plotted by Williams (1994, Figures 4a and 4c). The dominance of the Northern Hemisphere in the seasonal cycle of surface air temperature averaged over large symmetric latitude ranges (see our Figures 4c and 4d) is apparently related to the smaller amount of land in the opposite Southern Hemisphere: It is known that the

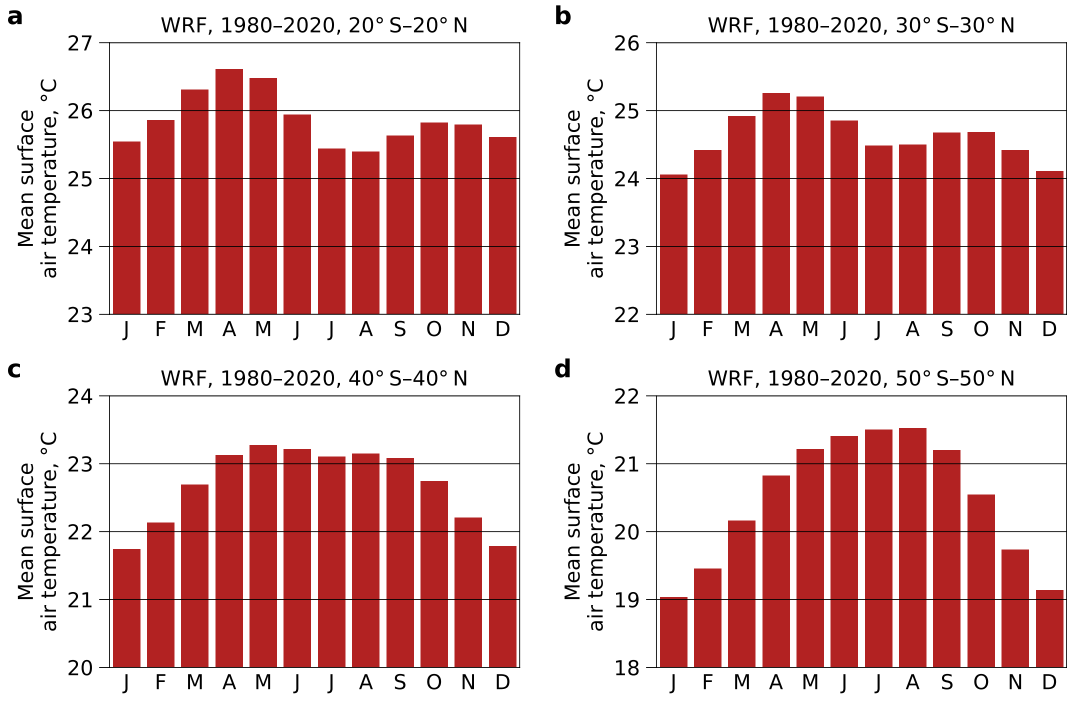

Figure 4. (a–d) Monthly mean values of air temperature at 2 m above the ground simulated for 1980–2020 using the WRF model, averaged over different latitude ranges, namely 20°S–20°N (a), 30°S–30°N (b), 40°S–40°N (c), and 50°S–50°N (d).

ocean is less responsive to changes in insolation than land areas owing to the large heat capacity and mobile nature of seawater.

The annual temperature cycles shown in Figure 4 provide a clear physical interpretation for the seasonal variation of the GEC shown in Figure 2. We have just noted that the asymmetrical distribution of land over the two hemispheres accounts for higher temperature values during the boreal summer, observed in Figures 4c and 4d. The same fact is likely to be the reason behind greater contributions to the GEC during the Northern Hemisphere summer, clearly seen in Figure 2: The greater amount of land in the Northern Hemisphere enhances the global convection intensity and the global amount of electrified clouds during the summer in this hemisphere, while during the boreal winter the global amount of electrified clouds is at a minimum. Note that in all panels of Figure 2 the highest PG value is reached in August, similarly to the highest mean temperature over 50°S–50°N in Figure 4d.

It is also remarkable that the pattern of a July minimum inside a flat maximum, observed in all three panels of Figure 2, is somewhat similar to the variation of Figure 4c, showing surface air temperature values averaged over 40°S–40°N. Given that contributions to the GEC at low and middle latitudes provide the main part of the total IP, and considering that these contributions must be correlated with insolation (and, by inference, with surface air temperatures as well), it is quite possible that their superposition in reality produces a variation similar to that of Figure 4c, with a local minimum amid the flat Northern Hemisphere summer maximum. In other words, it is likely that the seasonal behavior of the PG shown in Figure 2 actually represents the global signal.

Thus one can interpret the Vostok PG pattern, shown in Figure 2, as the result of a superposition of variation patterns for contributions from different latitude ranges, determined by the respective insolation cycles. Local insolation cycles influence (with a lag of about 1 month) not only surface air temperatures but also the convection intensity and the occurrence of electrified clouds: Higher insolation leads to higher surface air temperatures, more intense convection, and a greater number of electrified clouds. Thus the highest GEC intensity during the boreal summer can be regarded as a consequence of the prominent annual signal in nonequatorial insolation together with the greater amount of land in the Northern Hemisphere (as land regions are more responsive to changes in insolation than the ocean; cf. Figure 4d), while the small July minimum inside the main maximum can be considered a remnant of the semiannual signal, observed in equatorial insolation (cf. Figures 4a–4c).

Considering that nearly all of the GEC intensity is determined by contributions from low and middle latitudes, it is not surprising that the pattern of PG variation in Figure 2 has much in common with the average temperature patterns for 40°S–40°N (Figure 4c) and 50°S–50°N (Figure 4d). It is interesting to note that similar findings were earlier inferred in satellite observations of lightning flash rates: It turned out that average equatorial flash rates exhibit a strong semiannual signal, and if one includes higher latitudes, the two maxima inherited from the equatorial variation gradually merge into one Northern Hemisphere summer maximum (see Christian et al., 2003, Figures 7b and 7c). The variation of the global flash rate does not show a distinct local minimum inside this maximum, but such minimum is clearly seen around June and July at least for flash rates averaged over 30°S–30°N and probably also for larger latitude ranges straddling the equator (not plotted by Christian et al., 2003).

One should not think, however, that contributions to the GEC simply mirror surface air temperature values. If we sum the former and average the latter over certain regions lying within low and middle latitudes, the two quantities will indeed be correlated to a certain extent, but their variations need not be identical. At the same time the fact that certain patterns in air temperature and insolation variability are similar to the fair-weather PG variation derived from the Vostok data suggests that this PG variation may actually be representative of the real GEC intensity. The relationship between GEC parameters and air temperature was already discussed by Williams (1994) 30 years ago, but in the Vostok data we see such a relationship more clearly than ever before. We will further investigate this question in Part 2 of this study, where we will actually simulate contributions to the IP from different grid cells.

It is also interesting that the PG variation at Vostok, with a maximum during the Northern Hemisphere summer, reminds us of the typical seasonal PG variation observed on other continents in the Southern Hemisphere (Adlerman & Williams, 1996, Figure 1). As we remember, the latter variation is usually associated with the seasonal cycle of aerosols, which are unlikely to be that much important on the Antarctic Plateau. Of course, other parameters which influence air conductivity (the ion mobility, the ionization rate, and the ion-ion recombination coefficient) directly depend on the temperature (see, e.g., Tinsley & Zhou, 2006), but this dependence alone does not make PG values very sensitive to the temperature variability (cf. estimates of the effect of the ion mobility change with temperature in Burns et al., 2012). Therefore the similarity between the PG cycle at Vostok and PG cycles on other continents in the Southern Hemisphere presently does not appear to be a manifestation of some general property related to the PG in the Southern Hemisphere (although, of course, all these cycles are somehow ultimately related to the seasonal cycle of insolation).

One more consideration is worthy of note in this connection. We have just noted that in the Vostok PG behavior shown in Figure 2a there is a small local minimum in July amid the Northern Hemisphere summer maximum. This behavior is stable, the pattern repeating itself over time (see Figures 2b and 2c, showing the variation for 2006–2012 and 2013–2020 separately). In view of the fact that this July perturbation probably cannot be related to seasonal cycles of local meteorological parameters or aerosols but can be explained from the global perspective, we can expect the Vostok variation to be representative of the real GEC behavior.

5. Further Discussion

In this section we shall look once again at various seasonal variation patterns for the GEC based on both earlier data and the new results presented in Section 4.

5.1. Seasonal Variation Inferred From PG Measurements

In Section 2.2 we have pointed out that continental measurements of the fair-weather PG give us little information about the real seasonal variation in the GEC intensity. A reversal in the seasonal behavior of the PG between the two hemispheres (higher PG values in the local winter, lower PG values in the local summer), which was already known in the first half of the twentieth century, clearly implies the dominant role of local conductivity changes in the observed variations (see Equation 6).

According to the analysis by Adlerman and Williams (1996), one possible source of these conductivity changes is probably related to higher aerosol concentrations over the continents during local winters. Particular reasons for this phenomenon may include seasonal changes in anthropogenic aerosol production (more fossil fuels are consumed during the local winter), in atmospheric dispersion characteristics (lower mixed layer depth during the local winter results in higher aerosol concentrations), and in concentrations of wind-generated soil aerosols, depending on the seasonal cycle of wind velocities (see Adlerman & Williams, 1996, and references therein). All these factors could contribute to lower conductivity values and thus account for the observed higher PG values during local winters.

Besides aerosols, another factor which may contribute to local conductivity changes in continental locations is the radon emanated from the soil. This radon provides additional atmospheric ionization over the first few kilometers above the ground, thus increasing the conductivity near the Earth's surface (e.g., Tinsley & Zhou, 2006). Several studies reported significant seasonal variations in the radon-related ion-pair production rate (Hayashi et al., 2015; Holý et al., 1995; Hötzl & Winkler, 1994; Sesana et al., 2003); in particular, in the Northern Hemisphere the radon emanation is said to be at a minimum in the (local) summer and at a maximum in the winter. This would imply higher conductivity and lower PG values in winter for the Northern Hemisphere (which is the opposite of what we actually observe), which suggests that the effect of radon must be smaller in magnitude than changes due to aerosols. Let us also note that the conductivity depends on the air temperature (since so do the ion mobility and the coefficients describing ionization and ion-ion recombination; see Tinsley & Zhou, 2006); however, the part of the total variability which can be explained in this way is unlikely to be very large.

It is presently unclear whether it is possible to somehow eliminate the effects of aerosols and radon from the results of fair-weather PG measurements in continental locations. Only from PG measurements in clean oceanic or Antarctic locations can we hope to extract some meaningful information about the seasonal behavior of the GEC. In Section 2.2 we have cited two such data sets, namely the results of PG measurements on board the Carnegie and Maud research vessels in 1915–1929 and the results of PG measurements at the Vostok station in Antarctica in 1998–2001. In Section 4 we analyzed a more recent (and much longer) PG data series from Vostok, covering the period of 2006–2020 (with some gaps).

Regarding the seasonality in the Carnegie and Maud PG measurements, some uncertainty still remains. Early analysis by Parkinson and Torreson (1931) is now considered insufficiently accurate, but even studies of the last few decades inferred very different conclusions from these data. On the one hand, Adlerman and Williams (1996, Figure 7a) obtained a variation with a peak in July whose magnitude crucially depends on the criterion used to select fair-weather days (Figure 1a of this paper reproduces their variation for the case of the criterion based on neglecting PG values higher than 300 V/m). On the other hand, Harrison and Nicoll (2008, Figure 8e) arrived at greater PG values in the Northern Hemisphere winter on the basis of the Carnegie data alone.

We should note here that the original Carnegie data do not form a consistent time series, being nonuniformly distributed over UTC hours and seasons of the year; the instrumentation and technical procedures may also differ across the entire data set (see Ault & Mauchly, 1926; Torreson et al., 1946). Complete 24-hr PG records are available only for a small number of fair-weather days, and it is very likely that the details of data selection criteria and averaging procedures crucially influence the resulting variation. Reconciling the findings of different studies requires a more thorough analysis of the Carnegie and Maud data (if it is possible at all). Such an analysis, however, is beyond the scope of our present investigation.

We will now turn to the results of PG measurements at the Vostok station; we have already noted that Figure 1b, which is adapted from Burns et al. (2012, Figure 13) and based on the Vostok data for 1998–2001, and Figure 2a, which is based on the Vostok data for 2006–2020, at first sight appear to manifest different seasonal cycles. We will now investigate this question more thoroughly.

5.2. Possible Meteorological and Solar Wind Influences on the Seasonal Variation of the PG at Vostok

Apart from the fact that the Vostok data for 1998–2001 and for 2006–2020 were obtained with different field mills, Figures 1b and 2a are also essentially different in that we plotted the graph of the seasonal variation directly on the basis of the PG values recorded by the field mill, while Burns et al. (2012) attempted to adjust the original PG values to universal meteorological conditions and correct them for the influence of the solar wind. To illustrate the effect of such corrections, in Figure 5a we demonstrate the seasonal variation based on the unadjusted PG values measured at Vostok during 1998–2001; these values have been deduced from Burns et al. (2012, Table 2). To emphasize the role of PG adjustments, next to Figure 5a we once again reproduce Figure 1b, adapted from Burns et al. (2012, Figure 13), as Figure 5b.

Comparing Figures 5a and 5b, we see that both variations manifest three marked local maxima in March, in July, and in September. At the same time without corrections monthly PG values are clearly highest during the

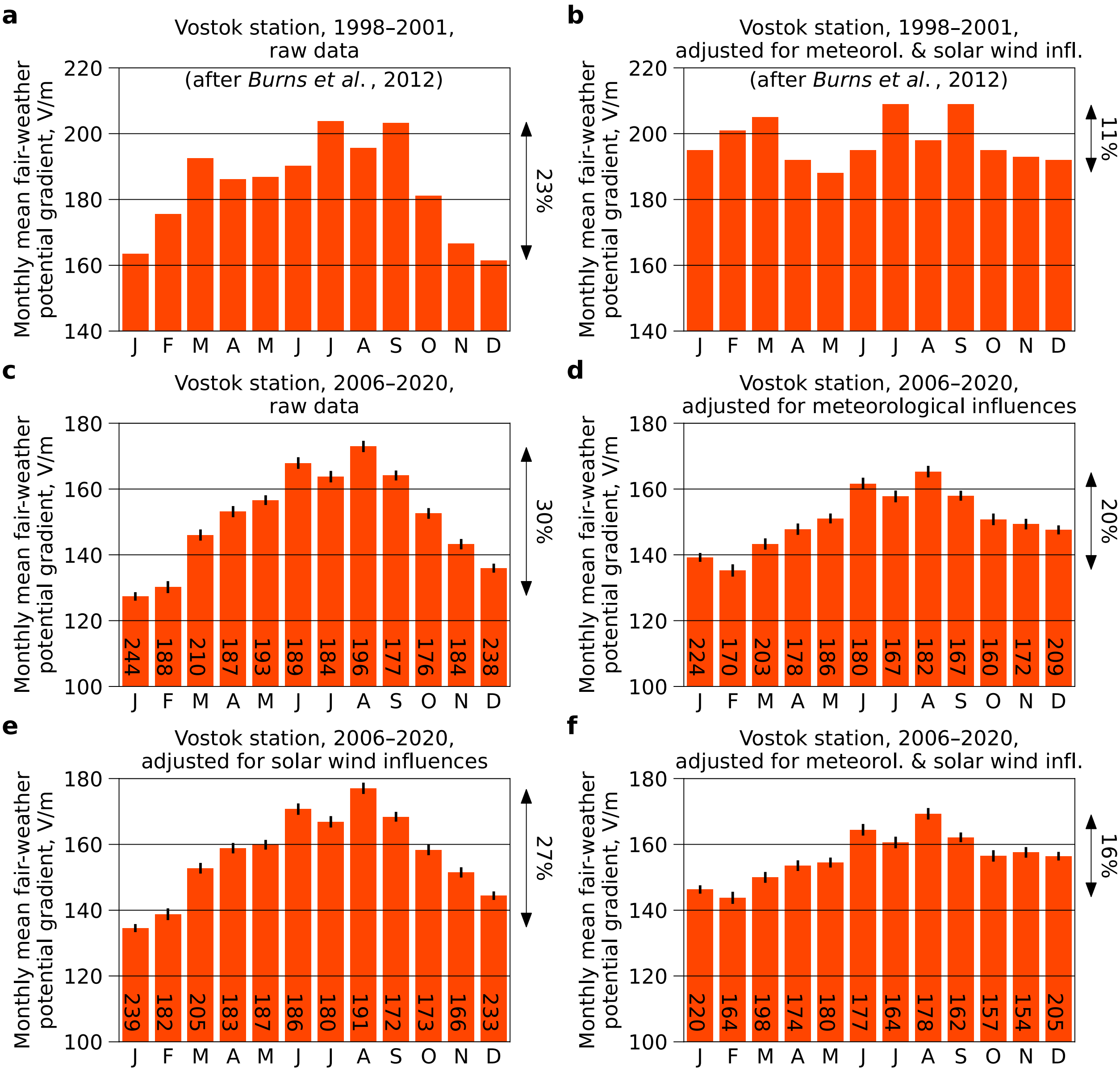

Figure 5. (a) Monthly mean values of the fair-weather PG according to measurements at the Vostok station in 1998–2001 (after Burns et al., 2012, Table 2). (b) Monthly mean PG values from the same data set adjusted for local meteorological and solar wind influences (after Burns et al., 2012, Table 2 and Figure 13; the same as Figure 1b). (c) Monthly mean values of the fair-weather PG according to measurements at the Vostok station in 2006–2020 (the same as Figure 2a). (d–f) Monthly mean PG values from the same data set adjusted for local meteorological influences (d), for solar wind influences (e), and for both these factors simultaneously (f; see the text for more details). Annotations inside the bars in panels (a, c, d) indicate the number of fair-weather days used to calculate the average values. Error bars in panels (a, c, d) demonstrate the values plus and minus one standard error. The double arrow to the right of each panel represents the peak-to-peak amplitude, and the number next to it gives this amplitude as a fraction of the annual mean.

Northern Hemisphere summer and lowest during the Northern Hemisphere winter, while adjustments of Burns et al. (2012) conspicuously reduced this difference between summer and winter; the peak-to-peak amplitude of the variation decreased from about 23% of the mean in the case of the unadjusted data to only 11% after the adjustments have been applied. To better understand the role of such adjustments, we will now apply somewhat similar corrections to the Vostok PG data for 2006–2020. We shall first consider local meteorological influences and solar wind influences separately and then estimate their combined effect.

To remove from the PG time series the variability related to local weather changes, we consider daily anomalies of the fair-weather PG and meteorological parameters at the station with respect to a 21-day running mean.

Computing coefficients for linear regression, we eventually obtain the following equation for adjusting PG values:

$$E_{\text{adjusted}}\ [\text{V/m}] = E\ [\text{V/m}] - (-0.51(T - \langle T \rangle)\ [^\circ\text{C}] + 2.82(W - \langle W \rangle)\ [\text{m/s}]), \tag{7}$$

where E, T, and W are the PG, air temperature, and wind velocity at Vostok, respectively, and angle brackets signify taking the long-term mean value. Technical details of the adjustment procedure are given in Supporting Information S1; here we confine ourselves to mentioning that our adjustment procedure is generally similar (although not exactly identical) to the one employed by Burns et al. (2012) for the earlier Vostok data.

The monthly mean PG values for 2006–2020 before and after applying the adjustment determined by Equation 7 are shown in Figures 5c and 5d, respectively (of course, Figure 5c just reproduces Figure 2a; the number of selected days in each month in Figure 5d is somewhat smaller owing to the occasional gaps in the weather data). We immediately see that the correction for weather variability results in a substantial reduction in the peak-to-peak amplitude of the variation (30% of the mean to 20%); at the same time the shape of the variation does not change much, and we still see the largest PG values during the Northern Hemisphere summer, and even the small July minimum inside the summer maximum persists.

Note, however, that simple adjustment procedures like the one described above have some shortcomings. For example, it is difficult to estimate the validity of linearly extrapolating the relationship between local fluctuations to the whole range of temperatures at Vostok; according to the analysis of Burns et al. (2012), the sensitivity of the PG to changes in temperature depends on the temperature itself. Even the mechanisms behind the supposed influence of meteorological factors on PG values are unclear; one such mechanism, relating this influence to modifying the local air conductivity, was already mentioned above, although it is unlikely to account for all of the observed relationship. Burns et al. (2012) have shown that conductivity changes related to the ion mobility variation with temperature are insufficient to explain the actual regression (they speculated about attributing the difference to a further variation in the ion mobility via possible changes in clustering of polar molecules on ions and ion attachment to aerosols or ice crystals). All this implies that we cannot be certain that correction procedures do not overestimate the real influence of various factors on the PG, and further research in this direction is needed (which is beyond the scope of this study).

Possible solar wind influences on Vostok PG values (in view of the high geomagnetic latitude of the station) have been discussed for several decades (Frank-Kamenetsky et al., 1999, 2001; Park, 1976b), and correcting these values for solar wind imposed potential differences has become a common practice (Burns et al., 2005, 2006, 2012, 2017). These potential differences locally disturb the IP value and thus also influence the air—Earth current density and the PG (e.g., Park, 1976a). Depending on solar wind parameters, the associated local IP perturbations over the polar caps can reach up to several tens of kV (e.g., Tinsley, 2022).

Polar cap potentials generally have their own seasonal patterns (see, e.g., Tinsley, 2024); these patterns are partially related to the geometry of the interplanetary magnetic field, in particular to the Rosenberg–Coleman effect (due to the tilt of the Earth's orbit with respect to the solar equatorial plane; see Rosenberg & Coleman, 1969) and to the Russell–McPherron effect (due to the tilt of the Earth's axis with respect to the solar equatorial plane; see Russell & McPherron, 1973). Besides, the thermospheric winds caused by auroral heating during magnetic storms produce the so-called ionospheric disturbance dynamo (Blanc & Richmond, 1980); in view of the greater frequency of magnetic storms around the equinoxes compared to the solstices, this effect can yield additional seasonally variable IP perturbations. However, over time spans of many years the seasonal patterns in solar wind imposed potential differences may to a large extent average out (owing to the Sun's magnetic field reversal during each 22-year Hale cycle).

Here we take into account the influence of the solar wind on Vostok PG values similarly to the effect of local meteorological factors. Using solar wind imposed potential differences calculated with the Weimer 2005 model (see Section 3.3), we compare daily anomalies for these potential differences and for the fair-weather PG at Vostok, compute linear regression coefficients, and finally arrive at the equation

$$E_{\text{adjusted}}\ [\text{V/m}] = E\ [\text{V/m}] - 0.74 V_{\text{sw}}\ [\text{kV}], \tag{8}$$

where V_{sw} is the solar wind imposed potential difference over Vostok. As before, technical details of the procedure which has led us to this equation are given in Supporting Information S1.

The monthly mean PG values for 2006–2020 corrected for solar wind influences via Equation 8 are shown in Figure 5e (as before with meteorological adjustments, owing to some gaps in solar wind data, the monthly numbers of selected days in Figure 5e are slightly smaller than their counterparts in Figure 5c). Comparing Figures 5c and 5e, we observe that the adjustment for solar wind influences does not substantially change the peak-to-peak amplitude of the variation (30% of the mean to 27%), and its shape also remains nearly identical.

If we simultaneously apply the adjustments given by Equations 7 and 8, we obtain the variation shown in Figure 5f (the monthly numbers of selected days become even smaller, since now we consider only formally selected fair-weather days for which both weather data and solar wind data are available). The peak-to-peak amplitude is now only 16% of the mean (nearly half as large as before the correction), and the variation itself is less pronounced; however, the largest PG values still occur during the Northern Hemisphere summer (with a maximum in August), and the July minimum is also clearly seen.

Thus we see that adjusting PG values for local meteorological and solar wind influences tends to substantially reduce the amplitude of the variation shown in Figure 2 and make the seasonal pattern more subtle but still identifiable. According to Figures 5c–5f, the main part of this amplitude reduction is due to the correction for local weather variability. This observation agrees with earlier findings that on the annual timescale air temperature provides the largest correction to Vostok PG values (the second largest being due to the solar wind; see Burns et al., 2012, Table 2).

5.3. Comparison of New and Earlier Seasonal Variation Patterns From Vostok

When we do not take any corrections into account, the variation based on the 1998–2001 Vostok data generally agrees with the variation for 2006–2020 in reaching higher values during the boreal summer (see Figures 5a and 5c). Greater PG values in 1998–2001 are probably due to different field mills employed (the two field mills were mounted at different altitudes, and the corresponding form factors were estimated independently). The most interesting distinction between seasonal variation patterns in the two data sets is the smaller relative peak-to-peak amplitude of the variation for 1998–2001 compared to that observed for 2006–2020; also, in the earlier data we do not see the behavior around July observed in the variation for 2006–2020 in Figure 2 (it actually manifests something similar with a lag of one month).

First of all, let us note that our own analysis also indicates a smaller peak-to-peak amplitude for 1998–2001. If we employ part of the 1-min time series for 1998–2004 published by Burns et al. (2010) and process these data using the same procedures that we used in the case of 10-s and 5-min Vostok PG data for 2006–2020 (see Section 3.1), we obtain the variation with a peak-to-peak amplitude of about 18% of the mean (it is shown in Figure S3 in Supporting Information S1). This value is of the same order as 23%, reported by Burns et al. (2012) for the unadjusted data, but not exactly the same owing to different data selection criteria.

There is actually no contradiction in the different seasonal behavior of the PG in 1998–2001 and 2006–2020. The bar plots for 1998–2001 are based on a substantially smaller number of days than those for 2006–2020 (compare annotations inside the bars in Figures 2b and 2c with those in Figure S3 in Supporting Information S1) and do not allow us to discuss very subtle effects. If we divide the range of 2006–2020 into 3-year periods (with more or less the same number of formally selected fair-weather days as in the 1998–2001 data set, which has large gaps in 2000), we obtain for these periods somewhat different variation patterns with peak-to-peak amplitudes lying in a range between 23% and 41% of the mean (the corresponding bar plots are shown in Figure S2 in Supporting Information S1). Moreover, we do not see a minimum in July for two of the five 3-year periods, which implies that this effect is indeed rather subtle and may not manifest itself over a period of 3–4 years.

Thus we see that the unusually small variation amplitude of 23%, inferred from Figure 5a (or 18%, according to the results of our own analysis, presented in Figure S3 in Supporting Information S1), does not generally contradict our long-term average value of 30% for the new data set. In Section 5.2 we have seen that these 30% reduce down to 16% if one adjusts PG values for meteorological and solar wind influences (see Figures 5c and 5f). In view of this fact it is not surprising that Burns et al. (2012) obtained an amplitude of about 11% after similar adjustments (see Figures 5a and 5b). It is interesting to note that based on the same data but without taking meteorological influences into account, Burns et al. (2005) had earlier reported a variation with a peak-to-peak amplitude of about 30% (see Burns et al., 2005, Table 5); however, this contradicts both the later analysis by Burns et al. (2012, Table 2) and our present findings and is likely to be the result of a different procedure employed to process the data.

On the whole, the variation inferred from the new Vostok data set seems to us more trustworthy, considering that it is based on a much longer time series and has proved to be stable over time (see Figures 2b and 2c); in addition, we have ascertained that its shape is not affected by meteorological adjustments and corrections for solar wind influences (see Figures 5c–5f). It is interesting to note that the boreal summer maximum of this variation qualitatively agrees with the summer PG maximum found by Adlerman and Williams (1996) in the Carnegie and Maud data (see Figure 1a), although the general shape of the variation is different; having said that, we once again point out that understanding the seasonality in the Carnegie data requires additional analysis.

5.4. Seasonal Variation Inferred From Air—Earth Current Measurements and IP Measurements

Next, we shall revisit the available results of air—Earth current measurements, summarized earlier in Section 2.3. First of all, let us note that the analysis of Section 4.2 supports our earlier remarks that seasonal variation patterns based on measurements at specific UTC hours need not be representative of the seasonal variability of the diurnal average GEC intensity: Since we search for a rather subtle effect, even slight nonuniform hour-to-hour changes may complicate the interpretation of observations. Therefore, here we shall refrain from interpreting seasonal patterns derived from data sets containing only current density values at specific UTC hours (e.g., Harrison & Ingram, 2005; Harrison & Nicoll, 2008); they should be compared with patterns in the results of PG measurements at precisely the same hours, which is beyond the scope of our present analysis.

There are presently only a few data sets based on long-term continuous measurements of the air—Earth current, which could make possible the computation of diurnal mean values. The 1930–1931 measurements at Kew Observatory (Scrase, 1933) yield a seasonal peak-to-peak amplitude equal to 114% of the mean (see Figure 1c). Given that any other data set which we have seen manifests a much smaller amplitude, it appears that the 1930–1931 Kew data require some adjustment in order to be deemed trustworthy (here we refrain from speculating about the possible origin of the apparent overestimation of the effect). It is still interesting, however, that the variation obtained by Scrase (1933) shows largest current density values during the boreal summer, with a maximum in August, which qualitatively agrees with the variation observed at Vostok (see Figure 2a).

The seasonal variation based on the 1965–1980 air—Earth current measurements at the National Observatory of Athens (Retalis, 1991), reproduced in Figure 1d, is also generally similar to the Vostok behavior, showing highest values in Northern Hemisphere summer and peaking in August; the most noticeable inconsistency between the two cycles is the prominent January maximum in the Athens data. The variation based on the 1977–1983 current measurements at the Mauna Loa Observatory (Adlerman & Williams, 1996, after W. E. Cobb), demonstrated in Figure 1e of this paper, also to some extent resembles the Vostok variation, except that the maximum value is attained in June and there is an additional marked minimum in April.

Owing to the smaller influence of local conductivity changes (compare Equations 5 and 6), the fair-weather air—Earth current density is generally thought to be more representative of actual global trends in the GEC intensity than the PG. However, the fact that different data sets yield dissimilar patterns implies that a precise measurement of this current is rather difficult. In addition, if we look at the diurnal variations inferred from current measurements at Kew (Scrase, 1933, Figure 6) or at Athens (Retalis, 1991, Figure 3) we shall ascertain that they only vaguely resemble the classical Carnegie curve; this further corroborates our claim that current measurements are not perfect in representing global trends. At the same time it is remarkable that all of the three data sets considered above indicate a higher GEC intensity during the Northern Hemisphere summer.

Apart from the Kew, Athens, and Mauna Loa data cited above, there are only a few continuous current density data sets referred to in the literature. Among the data sets considered by Hogg (1950) less than a half contain the results of continuous measurements, and none of them had been obtained in direct measurements (see Hogg, 1950, Tables 1 and 4); these data are not very reliable when it comes to predicting the average seasonal behavior of the GEC. There is a 1-year-long data set on the basis of earlier air—Earth current measurements at the Mauna Loa Observatory, which took place between September 1960 and August 1961 (Cobb & Phillips, 1962); this data set does not yield any clear annual variation (see Adlerman & Williams, 1996, Figure 4). The current density was continuously measured during 1964–1965 at the Brébeuf College Geophysical Observatory (Montréal, Canada); the published seasonal variations for 1964 and 1965 derived from these data are notably different (Gherzi, 1967, figures on p. 262), and it is unclear whether they are really based on true fair-weather days (the figure caption says "days without precipitation"). Anisimov and Shikhova (2014, Figure 3) presented a seasonal variation of the current density with a pronounced minimum in April and two notable maxima in October and January, obtained based on the results of continuous measurements at the Borok Geophysical Observatory (Borok, Russia) during 1999–2013; however, this pattern of variation had probably been influenced by some local effects (the authors mention the effect of snow and ice melting in spring), considering that monthly mean values of the current density are negatively correlated with their counterparts for the PG, which is hard to interpret from the global perspective. One of the longest continuous time series of air—Earth current measurements was recorded at Lerwick Observatory during 1978–1984; 15 UTC values from this data set have already been analyzed by Harrison and Nicoll (2008), but the seasonality in diurnal mean values has yet to be investigated.

Finally, we will make a few remarks about IP measurements. Although from a theoretical perspective the results of such measurements should most directly represent the global signal in the GEC, in practice measuring the IP is rather difficult and expensive, and there is not much data of this type available. The existing measurements were made at irregular intervals and at different UTC hours, often by means of different instrumentation and at different locations. In Section 2.4 we referred to the attempt by Markson (2007) to infer the seasonal behavior of the GEC from a compilation of available IP data sets (the resulting variation is reproduced here in Figure 1f), but the author himself notes that the values for November–January are less reliable owing to the nonuniform seasonal sampling of the available data and seeing that all of the existing December measurements had been made during the nuclear weapons testing period (when IP values were higher than usual). Also, we should note that although in the case of the bar plot shown in Figure 1f the IP values were diurnally normalized according to the Carnegie curve, this is still insufficient in the context of analyzing the annual variation. We have already noted several times that the actual shape of the diurnal variation of the GEC undergoes a substantial seasonal change (Burns et al., 2017); besides, this shape is additionally modified during El Niño and La Niña events (Slyunyaev, Frank-Kamenetsky, et al., 2021). In view of all this and considering the apparent subtlety of the GEC seasonality, we cannot infer any firm conclusions from the available results of IP measurements.

6. Conclusions

Numerous examples considered in this article demonstrate that the results of various observations can yield essentially different predictions concerning the seasonal behavior of the GEC. Notwithstanding that it is hard to draw firm conclusions from the data presently available to us, we can still make some important inferences. Let us now summarize the main findings of this study.

1. It is likely that there exists a stable annual cycle in the GEC intensity (just as the Carnegie curve is a stable cycle on the diurnal timescale, able to be seen when we average GEC parameters over a large number of days). For a number of reasons, this cycle is difficult to reliably determine from observations of atmospheric electrical parameters.
2. Since the shape of the diurnal variation of the GEC undergoes a prominent seasonal change, diurnal mean values of atmospheric electrical parameters and their values at specific UTC hours may manifest different seasonal behavior (in other words, diurnal aliasing can affect seasonal values and variations). Such discrepancies complicate the analysis of the results of IP measurements, some results of air—Earth current density measurements, and even the well-known PG data obtained on board the Carnegie research vessel.
3. Fair-weather PG measurements over continents are known to yield seasonal patterns dominated by annual cycles of local factors (especially aerosols, which influence air conductivity). This means that only PG measurements at clean locations (e.g., in the Antarctic or over the ocean) are suitable for analyzing the seasonal variation of the GEC.
4. PG measurements at the Vostok station in Antarctica predict the highest and lowest values of the diurnal mean GEC intensity during the Northern Hemisphere summer and winter, respectively. The highest PG value is attained in August; there is a small local minimum in July amid the flat summer maximum, which may be the result of adding together patterns of variation for contributions to the GEC of different latitude ranges (a similar behavior is observed for the average surface air temperature in the 40°S–40°N range). However, this effect is subtle and requires averaging over a sufficiently large number of years to be clearly seen.

5. The results of oceanic measurements on board the Carnegie ship do not form a consistent time series, and seasonal variation patterns derived from these data may crucially depend on data selection criteria and averaging procedures. According to the literature, the Carnegie data together with the data recorded on board the Maud ship, similarly to the Vostok data, indicate a summertime PG maximum, although there have also been reports of higher wintertime PG values inferred from the Carnegie data set.
6. Available results of continuous air—Earth current measurements generally indicate greater fair-weather current density values during the Northern Hemisphere summer and smaller values during the winter, in agreement with the Vostok PG variation. Seasonal behavior of the air—Earth current density measured at specific UTC hours can be somewhat different (the same behavior is observed for the PG at Vostok).
7. In general, it is highly likely that the actual seasonal variation in the diurnal mean GEC intensity has one pronounced maximum during the Northern Hemisphere summer and one pronounced minimum during the Northern Hemisphere winter (here we neglect possible local extrema of small magnitude). The dominance of the Northern Hemisphere in the resulting variation is apparently related to it having more land mass (just as it is dominating in the seasonal cycle of the surface air temperature averaged over the 40°S–40°N or 50°S–50°N latitude range).
8. The Vostok PG data further support the hypothesis linking the seasonal cycle of the GEC to the annual cycle of insolation (reflected by surface air temperatures). Both the Northern Hemisphere summer maximum in the Vostok PG and the small local minimum in July inside this maximum have a clear physical interpretation if we assume that contributions to the GEC in low and middle latitudes are correlated with local surface air temperatures.

Data Availability Statement

PG data from Vostok for 2006–2020, source codes, and scripts used to analyze the results and plot the images are available at https://zenodo.org/records/13898860 (Slyunyaev et al., 2025). Earlier Vostok PG data for 1998–2001 (Burns et al., 2010) were downloaded from https://data.aad.gov.au/metadata/ASAC_974_1. Weather data from Vostok can be downloaded, for example, from https://rp5.ru/Weather_archive_at_Vostok_Station. The Weimer 2005 model (Weimer, 2005a, 2005b) was downloaded from https://zenodo.org/records/2530324 (Weimer, 2019). Calculations with the Weimer 2005 model involved the hourly average OMNI data (King & Papitashvili, 2005; Papitashvili & King, 2020), obtained from the NASA GSFC Space Physics Data Facility's FTP service at https://omniweb.gsfc.nasa.gov/ow.html. The WRF-ARW model can be downloaded from https://www2.mmm.ucar.edu/wrf/users. Simulations with the WRF model used the ERA5 data (Hersbach et al., 2023), downloaded from the Copernicus Climate Change Service (C3S) Climate Data Store, so that their results contain modified C3S information 2021; neither the European Commission nor ECMWF is responsible for any use that may be made of the Copernicus information or data it contains.

Acknowledgments

The authors thank the reviewers of this article for many useful comments and suggestions. NNS, FGS, NVI, and EAM acknowledge the state assignment of the Institute of Applied Physics of the Russian Academy of Sciences (NNS, NVI, and EAM: project no. FFUF-2023-0004; NNS, FGS, and NVI: project no. FFUF-2022-0008). The authors are grateful to the Australian Antarctic Division and to Gary Burns, the chief investigator of the project "Atmospheric electrical circuits, weather and climate research," for their contribution to the development of instruments and software for collecting the electric field data at the Vostok station. Continuous registration and collection of the electric field data at Vostok was carried out by the specialists of the Russian Antarctic Expedition within the framework of the project "Integrated oceanological, climatic, glaciological, and geophysical studies of Antarctica and the Southern Ocean."

References

Adlerman, E. J., & Williams, E. R. (1996). Seasonal variation of the global electrical circuit. *Journal of Geophysical Research*, *101*(D23), 29679–29688. https://doi.org/10.1029/96JD01547

Anisimov, S., & Shikhova, N. (2014). Dynamical scaling of aeroelectrical field and current at middle latitudes. Paper presented at the 15th Int. Conf. on Atmospheric Electricity, Norman, Oklahoma, USA. https://www.nssl.noaa.gov/users/mansell/icae2014/preprints/Anisimov_15.pdf

Ault, J. P., & Mauchly, S. J. (1926). Atmospheric electric results obtained aboard the Carnegie, 1915–1921. In *Ocean magnetic and electric observations, 1915–1921* (pp. 195–286). Carnegie Institution of Washington. Retrieved from https://archive.org/details/oceanmagneticele00carn

Bhartendu. (1971a). Correlations of electric potential gradients at land stations and their implication on the classical picture of atmospheric electricity. *Pure and Applied Geophysics*, *84*(1), 13–26. https://doi.org/10.1007/BF00875447

Bhartendu. (1971b). Atmospheric electricity measurements at Toronto. *Atmosphere*, *9*(1), 16–25. Retrieved from https://cmosarchives.ca/Atmosphere/a0901.pdf

Blakeslee, R. J., Mach, D. M., Bateman, M. G., & Bailey, J. C. (2014). Seasonal variations in the lightning diurnal cycle and implications for the global electric circuit. *Atmospheric Research*, *135–136*, 228–243. https://doi.org/10.1016/j.atmosres.2012.09.023

Blanc, M., & Richmond, A. (1980). The ionospheric disturbance dynamo. *Journal of Geophysical Research*, *85*(A4), 1669–1686. https://doi.org/10.1029/JA085iA04p01669

Builder, G. (1929). The effect of condensation-nuclei in atmospheric-electric observations. *Terrestrial Magnetism and Atmospheric Electricity*, *34*(4), 281–286. https://doi.org/10.1029/TE034i004p00281

Burns, G. B., Papitashvili, V., Frank-Kamanetsky, A. V., Troshichev, O., & Bering, E. A. (2010). Electric field mill measurements, ver. 1 [Dataset]. *Australian Antarctic Data Centre*. https://doi.org/10.4225/15/588811d206493

Burns, G. B., Frank-Kamenetsky, A. V., Tinsley, B. A., French, W. J., Grigioni, P., Camporeale, G., & Bering, E. A. (2017). Atmospheric global circuit variations from Vostok and Concordia electric field measurements. *Journal of the Atmospheric Sciences*, *74*(3), 783–800. https://doi.org/10.1175/JAS-D-16-0159.1

Burns, G. B., Frank-Kamenetsky, A. V., Troshichev, O. A., Bering, E. A., & Reddell, B. D. (2005). Interannual consistency of bi-monthly differences in diurnal variations of the ground-level, vertical electric field. *Journal of Geophysical Research*, *110*(D10), D10106. https://doi.org/10.1029/2004JD005469

Burns, G. B., Tinsley, B. A., Frank-Kamenetsky, A. V., Troshichev, O. A., French, W. J. R., & Klekociuk, A. R. (2012). Monthly diurnal global atmospheric circuit estimates derived from Vostok electric field measurements adjusted for local meteorological and solar wind influences. *Journal of the Atmospheric Sciences*, *69*(6), 2061–2082. https://doi.org/10.1175/JAS-D-11-0212.1

Burns, G. B., Tinsley, B. A., Klekociuk, A. R., Troshichev, O. A., Frank-Kamenetsky, A. V., Duldig, M. L., et al. (2006). Antarctic polar plateau vertical electric field variations across heliocentric current sheet crossings. *Journal of Atmospheric and Solar-Terrestrial Physics*, *68*(6), 639–654. https://doi.org/10.1016/j.jastp.2005.10.008

Chalmers, J. A. (1967). *Atmospheric electricity* (2nd ed.). Pergamon Press.

Chree, C., & Watson, R. E. (1924). Atmospheric pollution and potential gradient at Kew observatory, 1921 and 1922. *Proceedings of the Royal Society of London A*, *105*(731), 311–333. https://doi.org/10.1098/rspa.1924.0022

Christian, H. J., Blakeslee, R. J., Boccippio, D. J., Boeck, W. L., Buechler, D. E., Driscoll, K. T., et al. (2003). Global frequency and distribution of lightning as observed from space by the Optical Transient Detector. *Journal of Geophysical Research*, *108*(D1), 4005. https://doi.org/10.1029/2002JD002347

Cobb, W. E., & Phillips, B. B. (1962). *Atmospheric electric results at Mauna Loa observatory*. (Technical Paper no. 46). U.S. Department of Commerce, Weather Bureau.

Dolezalek, H. (1960a). Zur Berechnung des luftelektrischen Stromkreises II: Über die Gültigkeit des Ohmschen Gesetzes in der Atmosphäre. *Geofisica Pura e Applicata*, *45*(1), 273–297. https://doi.org/10.1007/BF01996595

Dolezalek, H. (1960b). Zur Berechnung des luftelektrischen Stromkreises III: Kontrolle des Ohmschen Gesetzes durch Messung. *Geofisica Pura e Applicata*, *46*(1), 125–144. https://doi.org/10.1007/BF02001103

Exner, F. (1900). Summary of the results of recent investigations in atmospheric electricity. *Terrestrial Magnetism and Atmospheric Electricity*, *5*(4), 167–174. https://doi.org/10.1029/TE005i004p00167

Fischer, H. J. (1962). *Die elektrische Spannung zwischen Ionosphäre und Erde* (Ph. D. Thesis). Technischen Hochschule Stuttgart.

Frank-Kamenetsky, A. V., Burns, G. B., Troshichev, O. A., Papitashvili, V. O., Bering, E. A., & French, W. J. R. (1999). The geoelectric field at Vostok, Antarctica: Its relation to the interplanetary magnetic field and the cross polar cap potential difference. *Journal of Atmospheric and Solar-Terrestrial Physics*, *61*(18), 1347–1356. https://doi.org/10.1016/S1364-6826(99)00089-9

Frank-Kamenetsky, A. V., Troshichev, O. A., Burns, G. B., & Papitashvili, V. O. (2001). Variations of the atmospheric electric field in the near-pole region related to the interplanetary magnetic field. *Journal of Geophysical Research*, *106*(A1), 179–190. https://doi.org/10.1029/2000JA900058

Gherzi, E. E. (1967). Atmospheric electricity at Brébeuf college geophysical observatory in Montréal, Canada. *Pure and Applied Geophysics*, *67*(1), 239–265. https://doi.org/10.1007/BF00880582

Halliday, E. C. (1933). Variations in the electric field in the atmosphere measured in Johannesburg, South Africa, during 1929 and 1930. *Terrestrial Magnetism and Atmospheric Electricity*, *38*(1), 37–53. https://doi.org/10.1029/TE038i001p00037

Harrison, R. G. (2003). Twentieth-century atmospheric electrical measurements at the observatories of Kew, Eskdalemuir and Lerwick. *Weather*, *58*(1), 11–19. https://doi.org/10.1256/wea.239.01

Harrison, R. G., & Ingram, W. J. (2005). Air–earth current measurements at Kew, London, 1909–1979. *Atmospheric Research*, *76*(1–4), 49–64. https://doi.org/10.1016/j.atmosres.2004.11.022

Harrison, R. G., & Nicoll, K. A. (2008). Air-earth current density measurements at Lerwick; implications for seasonality in the global electric circuit. *Atmospheric Research*, *89*(1–2), 181–193. https://doi.org/10.1016/j.atmosres.2008.01.008

Harrison, R. G., Nicoll, K. A., Joshi, M., & Hawkins, E. (2022). Empirical evidence for multidecadal scale global atmospheric electric circuit modulation by the El Niño-Southern Oscillation. *Environmental Research Letters*, *17*(12), 124048. https://doi.org/10.1088/1748-9326/aca68c

Hayakawa, M., Galuk, Y. P., & Nickolaenko, A. P. (2023). Integrated Schumann resonance intensity as an indicator of the global thunderstorm activity. *Geosciences*, *13*(6), 177. https://doi.org/10.3390/geosciences13060177

Hayashi, K., Yasuoka, Y., Nagahama, H., Muto, J., Ishikawa, T., Omori, Y., et al. (2015). Normal seasonal variations for atmospheric radon concentration: A sinusoidal model. *Journal of Environmental Radioactivity*, *139*, 149–153. https://doi.org/10.1016/j.jenvrad.2014.10.007

Hersbach, H., Bell, B., Berrisford, P., Biavati, G., Horányi, A., Muñoz Sabater, J., et al. (2023). ERA5 hourly data on pressure levels from 1940 to present [Dataset]. *Copernicus Climate Change Service (C3S) Climate Data Store (CDS)*. https://doi.org/10.24381/cds.bd0915c6

Hogg, A. R. (1950). Air-earth current observations in various localities. *Archiv für Meteorologie, Geophysik und Bioklimatologie, Serie A*, *3*(1–2), 40–55. https://doi.org/10.1007/BF02247517

Holý, K., Böhm, R., Polášková, A., & Štelina, J. (1995). Variations of ^{222}Rn concentration in outdoor atmosphere and in soil air. In *Proceedings of the 19th radiation hygiene days* (pp. 129–131). Society of Nuclear Medicine and Radiation Hygiene of Slovak Medical Association. Retrieved from https://inis.iaea.org/collection/NCLCollectionStore/_Public/28/074/28074048.pdf

Hötzl, H., & Winkler, R. (1994). Long-term variation of outdoor radon equilibrium equivalent concentration. *Radiation and Environmental Biophysics*, *33*(4), 381–392. https://doi.org/10.1007/BF01210459

Kasemir, H. W. (1956). Zur Strömungstheorie des luftelektrischen Feldes III: Der Austauschgenerator. *Archiv für Meteorologie, Geophysik und Bioklimatologie, Serie A*, *9*(3), 357–370. https://doi.org/10.1007/BF02247454

King, J. H., & Papitashvili, N. E. (2005). Solar wind spatial scales in and comparisons of hourly Wind and ACE plasma and magnetic field data. *Journal of Geophysical Research*, *110*(A2), A02104. https://doi.org/10.1029/2004JA010649

Kozlov, A. V., Slyunyaev, N. N., Ilin, N. V., Sarafanov, F. G., & Frank-Kamenetsky, A. V. (2023). The effect of the Madden–Julian Oscillation on the global electric circuit. *Atmospheric Research*, *284*, 106585. https://doi.org/10.1016/j.atmosres.2022.106585

Lavigne, T., Liu, C., Deierling, W., & Mach, D. (2017). Relationship between the global electric circuit and electrified cloud parameters at diurnal, seasonal, and interannual timescales. *Journal of Geophysical Research: Atmospheres*, *122*(16), 8525–8542. https://doi.org/10.1002/2016JD026442

Mach, D. M., Blakeslee, R. J., & Bateman, M. G. (2011). Global electric circuit implications of combined aircraft storm electric current measurements and satellite-based diurnal lightning statistics. *Journal of Geophysical Research*, *116*(D5), D05201. https://doi.org/10.1029/2010JD014462

Mareeva, O. V., Mareev, E. A., Kalinin, A. V., & Zhidkov, A. A. (2011). Convective generator in the global electric circuit: Analytical approach and numerical consideration. (Paper presented at the 14th Int. Conf. on Atmospheric Electricity, Rio de Janeiro, Brazil).

Markson, R. (1986). Tropical convection, ionospheric potentials and global circuit variation. *Nature*, *320*(6063), 588–594. https://doi.org/10.1038/320588a0

Markson, R. (2007). The global circuit intensity: Its measurement and variation over the last 50 years. *Bulletin of the American Meteorological Society*, *88*(2), 223–241. https://doi.org/10.1175/BAMS-88-2-223

Mauchly, S. J. (1921). Note on the diurnal variation of the atmospheric-electric potential-gradient. *Physical Review*, *18*(2), 161–162. https://doi.org/10.1103/PhysRev.18.85

Mauchly, S. J. (1923). On the diurnal variation of the potential gradient of atmospheric electricity. *Terrestrial Magnetism and Atmospheric Electricity*, *28*(3), 61–81. https://doi.org/10.1029/TE028i003p00061

Mühleisen, R. (1971). New determination of the air-earth current over the ocean and measurements of ionosphere potentials. *Pure and Applied Geophysics*, *84*(1), 112–115. https://doi.org/10.1007/BF00875459

Mühleisen, R. (1977). The global circuit and its parameters. In H. Dolezalek & R. Reiter (Eds.), *Electrical processes in atmospheres* (pp. 467–476). Steinkopff. https://doi.org/10.1007/978-3-642-85294-7_73

Papitashvili, N. E., & King, J. H. (2020). OMNI hourly data [Dataset]. *NASA Space Physics Data Facility*. https://doi.org/10.48322/1shr-ht18

Park, C. G. (1976a). Downward mapping of high-latitude ionospheric electric fields to the ground. *Journal of Geophysical Research*, *81*(1), 168–174. https://doi.org/10.1029/JA081i001p00168

Park, C. G. (1976b). Solar magnetic sector effects on the vertical atmospheric electric field at Vostok, Antarctica. *Geophysical Research Letters*, *3*(8), 475–478. https://doi.org/10.1029/GL003i008p00475

Parkinson, W. C., & Torreson, O. W. (1931). The diurnal variation of the electric potential of the atmosphere over the oceans. *UGGI Bulletin*, *8*, 340–345.

Powers, J. G., Klemp, J. B., Skamarock, W. C., Davis, C. A., Dudhia, J., Gill, D. O., et al. (2017). The Weather Research and Forecasting model: Overview, system efforts, and future directions. *Bulletin of the American Meteorological Society*, *98*(8), 1717–1737. https://doi.org/10.1175/BAMS-D-15-00308.1

Price, C., & Melnikov, A. (2004). Diurnal, seasonal and inter-annual variations in the Schumann resonance parameters. *Journal of Atmospheric and Solar-Terrestrial Physics*, *66*(13–14), 1179–1185. https://doi.org/10.1016/j.jastp.2004.05.004

Retalis, D. A. (1991). Study of the air-earth electrical current density in Athens. *Pure and Applied Geophysics*, *136*(2–3), 217–233. https://doi.org/10.1007/BF00876374

Rosenberg, R. L., & Coleman, P. J., Jr. (1969). Heliographic latitude dependence of the dominant polarity of the interplanetary magnetic field. *Journal of Geophysical Research*, *74*(24), 5611–5622. https://doi.org/10.1029/JA074i024p05611

Russell, C. T., & McPherron, R. L. (1973). Semiannual variation of geomagnetic activity. *Journal of Geophysical Research*, *78*(1), 92–108. https://doi.org/10.1029/JA078i001p00092

Rycroft, M. J., Harrison, R. G., Nicoll, K. A., & Mareev, E. A. (2008). An overview of Earth's global electric circuit and atmospheric conductivity. *Space Science Reviews*, *137*(1–4), 83–105. https://doi.org/10.1007/s11214-008-9368-6

Scrase, F. J. (1933). *The air-Earth current at Kew Observatory*. H. M. Stationery Off. Retrieved from https://digital.nmla.metoffice.gov.uk/IO_78a2c258-0c8c-4eed-9654-855eec72bc81

Sesana, L., Caprioli, E., & Marcazzan, G. (2003). Long period study of outdoor radon concentration in Milan and correlation between its temporal variations and dispersion properties of atmosphere. *Journal of Environmental Radioactivity*, *65*(2), 147–160. https://doi.org/10.1016/S0265-931X(02)00093-0

Skamarock, W. C., Klemp, J. B., Dudhia, J., Gill, D. O., Liu, Z., Berner, J., et al. (2019). A description of the advanced research WRF version 4. (NCAR Technical Note NCAR/TN-556+STR). https://doi.org/10.5065/1dfh-6p97

Slyunyaev, N. N., Sarafanov, F., Ilin, N., Mareev, E., Volodin, E., Frank-Kamenetsky, A., & Williams, E. (2025). Data and code for articles on the seasonal variation of the DC global electric circuit [Dataset]. *Zenodo*. https://doi.org/10.5281/zenodo.13898860

Slyunyaev, N. N., Frank-Kamenetsky, A. V., Ilin, N. V., Sarafanov, F. G., Shatalina, M. V., Mareev, E. A., & Price, C. G. (2021). Electric field measurements in the Antarctic reveal patterns related to the El Niño—Southern oscillation. *Geophysical Research Letters*, *48*(21), e2021GL095389. https://doi.org/10.1029/2021GL095389

Slyunyaev, N. N., Ilin, N. V., Mareev, E. A., & Price, C. G. (2021). The global electric circuit land–ocean response to the El Niño—Southern oscillation. *Atmospheric Research*, *260*, 105626. https://doi.org/10.1016/j.atmosres.2021.105626

Sverdrup, H. U. (1926). Scientific work of the Maud expedition, 1922–1925. *The Scientific Monthly*, *22*(5), 400–410. Retrieved from https://www.jstor.org/stable/7648

Tacza, J., Nicoll, K. A., & Macotela, E. (2022). Periodicities in fair weather potential gradient data from multiple stations at different latitudes. *Atmospheric Research*, *276*, 106250. https://doi.org/10.1016/j.atmosres.2022.106250

Thomson, W. (1860). Atmospheric electricity. In J. P. Nichol (Ed.), *A cyclopaedia of the physical sciences* (2nd ed., pp. 267–274). Richard Griffin. Retrieved from https://archive.org/details/b21496079

Thomson, W. (1884). Atmospheric electricity. In *Reprint of papers on electrostatics and magnetism* (2nd ed., pp. 192–239). Macmillan. Retrieved from https://archive.org/details/reprintofpaperso00kelvrich

Tinsley, B. A. (2022). Uncertainties in evaluating global electric circuit interactions with atmospheric clouds and aerosols, and consequences for radiation and dynamics. *Journal of Geophysical Research: Atmospheres*, *127*(5), e2021JD035954. https://doi.org/10.1029/2021JD035954

Tinsley, B. A. (2024). The influence of the solar wind electric and magnetic fields on the latitude and temporal variations of the current density, J_Z, of the global electric circuit, with relevance to weather and climate. *Journal of Atmospheric and Solar-Terrestrial Physics*, *265*, 106355. https://doi.org/10.1016/j.jastp.2024.106355

Tinsley, B. A., & Zhou, L. (2006). Initial results of a global circuit model with variable stratospheric and tropospheric aerosols. *Journal of Geophysical Research*, *111*(D16), D16205. https://doi.org/10.1029/2005JD006988

Torreson, O. W., Parkinson, W. C., Gish, O. H., & Wait, G. R. (1946). *Ocean atmospheric-electric results (Scientific results of Cruise VII of the Carnegie during 1928–1929 under command of captain J. P. Ault, Oceanography—III)*. Carnegie Institution of Washington. Retrieved from https://archive.org/details/oceanatmospheric00carn

Wait, G. R. (1927). Preliminary note on the effect of dust, smoke, and relative humidity upon the potential gradient and the positive and negative conductivities of the atmosphere. *Terrestrial Magnetism and Atmospheric Electricity*, *32*(1), 31–35. https://doi.org/10.1029/TE032i001p00031

Weimer, D. R. (2019). Weimer 2005 ionospheric electric potential model for IDL [Software]. *Zenodo*. https://doi.org/10.5281/zenodo.2530324

Weimer, D. R. (2005a). Improved ionospheric electrodynamic models and application to calculating Joule heating rates. *Journal of Geophysical Research*, *110*(A5), A05306. https://doi.org/10.1029/2004JA010884

Weimer, D. R. (2005b). Predicting surface geomagnetic variations using ionospheric electrodynamic models. *Journal of Geophysical Research*, *110*(A12), A12307. https://doi.org/10.1029/2005JA011270

Whipple, F. J. W. (1929a). On the association of the diurnal variation of electric potential gradient in fine weather with the distribution of thunderstorms over the globe. *Quarterly Journal of the Royal Meteorological Society*, *55*(229), 1–18. https://doi.org/10.1002/qj.49705522902

Whipple, F. J. W. (1929b). Potential gradient and atmospheric pollution: The influence of "summer time". *Quarterly Journal of the Royal Meteorological Society*, *55*(232), 351–362. https://doi.org/10.1002/qj.49705523206

Whipple, F. J. W., & Scrase, F. J. (1936). *Point discharge in the electric field of the Earth: An analysis of continuous records obtained at Kew Observatory*. H. M. Stationery Off. Retrieved from https://digital.nmla.metoffice.gov.uk/IO_efb7fd62-a542-4266-aac6-cbdeae3311b6

Willett, J. C. (1979). Fair weather electric charge transfer by convection in an unstable planetary boundary layer. *Journal of Geophysical Research*, *84*(C2), 703–718. https://doi.org/10.1029/JC084iC02p00703

Williams, E. R., & Mareev, E. (2014). Recent progress on the global electrical circuit. *Atmospheric Research*, *135–136*, 208–227. https://doi.org/10.1016/j.atmosres.2013.05.015

Williams, E. R. (1994). Global circuit response to seasonal variations in global surface air temperature. *Monthly Weather Review*, *122*(8), 1917–1929. https://doi.org/10.1175/1520-0493(1994)122⟨1917:GCRTSV⟩2.0.CO;2

Williams, E. R. (2009). The global electrical circuit: A review. *Atmospheric Research*, *91*(2–4), 140–152. https://doi.org/10.1016/j.atmosres.2008.05.018

Williams, E. R., & Heckman, S. J. (1993). The local diurnal variation of cloud electrification and the global diurnal variation of negative charge on the Earth. *Journal of Geophysical Research*, *98*(D3), 5221–5234. https://doi.org/10.1029/92JD02642

Williams, E. R., & Sátori, G. (2004). Lightning, thermodynamic and hydrological comparison of the two tropical continental chimneys. *Journal of Atmospheric and Solar-Terrestrial Physics*, *66*(13–14), 1213–1231. https://doi.org/10.1016/j.jastp.2004.05.015

Wilson, C. T. R. (1921). Investigations on lightning discharges and on the electric field of thunderstorms. *Philosophical Transactions of the Royal Society of London A*, *221*, 73–115. https://doi.org/10.1098/rsta.1921.0003

Supporting Information for "The seasonal variation of the direct current global electric circuit: Part 1. A new analysis based on long-term measurements in Antarctica"

Nikolay N. Slyunyaev[1], Fedor G. Sarafanov[1], Nikolay V. Ilin[1],
Evgeny A. Mareev[1], Evgeny M. Volodin[2],
Alexander V. Frank-Kamenetsky[3], and Earle R. Williams[4]

[1]Institute of Applied Physics, Russian Academy of Sciences, Nizhny Novgorod, Russia

[2]Institute of Numerical Mathematics, Russian Academy of Sciences, Moscow, Russia

[3]Arctic and Antarctic Research Institute, St. Petersburg, Russia

[4]Parsons Laboratory of the Department of Civil and Environmental Engineering, Massachusetts Institute of Technology, Cambridge, MA, USA

Contents of this file

Introduction

This file contains technical details behind processing potential gradient (PG) data from the Vostok station, correcting PG values for the variability of meteorological factors and solar wind imposed potentials, and simulating surface air temperature values with the Weather Research and Forecasting model (WRF). The file also includes three supplementary figures for the article.

Taking into account the variation of the form factor for the field mill at Vostok

The rotating-dipole field mill at Vostok, which operated during 2006–2020, was supported by a metal pole. To remove the disturbance of the electric field caused by this metal pole, the recorded PG values must be divided by a suitably chosen form factor.

At the end of 2005, when the field mill had just been installed, the form factor value was determined to be close to 3. This value was established in a series of experiments involving another field mill placed at some distance from the main one and two wires creating an external electric field around the main field mill (one lying at the ground, the other stretched above the field mill). In the absence of external electric field (and the wires) simultaneous measurements with the two field mills yielded the ratio of their form factors; then the form factors themselves were inferred by setting different voltages between the two wires and simultaneously measuring the total electric field (i.e. the sum of the fair-weather field and the external field produced by the wires) with the first field mill and the fair-weather electric field alone with the second field mill.

At the end of 2005 the height of the metal pole supporting the field mill was approximately 2.95 m above the ground, and the experiments described above yielded that the actual electric field was then overestimated by a factor of approximately 3. However, since that moment the height of the metal pole has been gradually decreasing owing to the constant accumulation of wind-drifted snow, and typical PG values recorded by the field mill have been decreasing accordingly. According to direct measurements recently performed at Vostok, in December 2024 the height of the pole was about 1.75 m.

To take into account the apparent reduction of the form factor over the years, we have created a simple finite-element model calculating electric fields in the vicinity of a metal pole equipotential with the surface. Setting the electric field far from the pole equal to 100 V/m and assuming the pole diameter to be 10 cm, we calculated the vertical component of the downward electric field at the height of top of the pole 25 cm away from its center. In this way we obtained 178 V/m for a 2.95 m high pole and 143 V/m for a 1.75 m high pole; this means that in our idealized problem the form factor would decrease from 1.78 down to 1.43. Moreover, additional calculations indicated that in the range between these values the form factor would change nearly linearly with the pole height.

The real situation is more complicated, as the field mill itself further disturbs the electric field. However, we did not explicitly solve a more complicated problem (in any case, it would be difficult to take into account all the peculiarities of the real field mill) and simply assumed that even though a simplified problem described above underestimates absolute values of the form factor, it more or less correctly predicts its rate of change with respect to the pole height. This means that the form factor of 3 determined in experiments for the 2.95 m high pole must decrease down to $3 \cdot (1.43/1.78) \approx 2.4$ for the 1.75 m high pole, while the intermediate values can be estimated by means of a linear interpolation.

Based on the remarks given above, in actual calculations we required the form factor to decrease from 3 on 1 January 2006 to 2.4 on 1 December 2024. Assuming a uniform increase in snow depth, we linearly interpolated missing values for each day during 2006–2020, when the field mill had been operating. In particular, the value for 31 December 2020 (the last day of the period which we consider) turned out to be about 2.52, which is 16% smaller than the initial value of 3.

Simulating surface air temperature with the Weather Research and Forecasting model

To simulate the distribution of surface air temperature over the Earth's surface, we used the weather forecasting model WRF (e.g., Powers et al., 2017), which had been run globally on a $1^\circ \times 1^\circ$ latitude-longitude grid to simulate the atmospheric dynamics during 1980–2020, with meteorological reanalysis data used as initial conditions in model runs.

More precisely, we employed version 4.3 of the Advanced Research WRF (ARW) solver (Skamarock et al., 2019), which was run globally on a $1^\circ \times 1^\circ$ latitude-longitude grid with 51 altitude levels from the Earth's surface to the 10-mbar level and time steps of 150 s. The following physics schemes for the WRF were chosen: mp_physics = 2, ra_lw_physics = 4, ra_sw_physics = 4, radt = 30, sf_sfclay_physics = 1, sf_surface_physics = 2, bl_pbl_physics = 1, and cu_physics = 2. We used the hybrid sigma-pressure coordinate, a hydrostatic solver, and polar filtering for latitudes greater than 60°.

To initialize the WRF, we used the ERA5 data on pressure levels (Hersbach et al., 2023); ERA5 stands for the fifth generation ECMWF (European Centre for Medium-Range Weather Forecasts) reanalysis for the global climate and weather. We carried out 48-hour free runs of the model starting at 0 UTC and 12 UTC on every third day from 31 December 1979 to 28 December 2020. In each model run we restricted our attention to the 24-hour interval between 18 and 42 hours since the model initiation, as the model needs some time to achieve the correct reproduction of the data absent in initial conditions. Then for every third day from 1 January 1980 to 29 December 2020 we calculated diurnal mean values of surface air temperature (or, more precisely, air temperature at 2 m) in each grid cell by averaging the simulated temperature over the two aforementioned 24-hour intervals corresponding to the day in question (i.e. over those two 24-hour intervals which for the most part lie within the particular day).

Estimating the solar wind imposed potential difference over Vostok

To estimate the variation of the solar wind imposed potential difference above Vostok, we employed the Weimer 2005 model (Weimer, 2005a, 2005b, 2019). It is an empirical model evaluating ionospheric potential distribution over high-latitude regions on the basis of interplanetary magnetic field and solar wind parameters. Calculations covered the entire period of 2006–2020 and were performed for a point with coordinates 78.46° S, 106.84° E, which approximately corresponds to the location of the station.

As input for the Weimer 2005 model, we used the near-Earth solar wind magnetic field and plasma parameters taken from NASA (National Aeronautics and Space Administration) GSFC (Goddard Space Flight Center) Space Physics Data Facility's OMNI data set (King & Papitashvili, 2005; Papitashvili & King, 2020). The required parameters include the interplanetary magnetic field components, the solar wind velocity, and the solar wind number density. For our calculations we used hourly averaged values of these parameters (over 0–1 UTC, 1–2 UTC and so on for each day); the magnetic dipole tilt angle was computed by the model for the middle of the corresponding hour (0:30 UTC, 1:30 UTC etc.). Thus we calculated the value of the electric potential over 78.46° S, 106.84° E for each hour within 2006–2020 (except for those few days where the OMNI data were not completely available).

Adjustment of the Vostok potential gradient data for local meteorological influences

To remove from the PG time series the variability related to local weather changes, we employ the following simple procedure.

First, for each day we compute average values of air temperature, air pressure and wind velocity at the Vostok station (to this end, we use actual weather information from the station). Second, we select from the PG data set all formally determined fair-weather days for which the meteorological parameters have also been recorded. Next, we compute daily anomalies of the PG and meteorological parameters by subtracting the mean values over symmetric 21-day intervals around each day (with only formally selected fine days with weather data available taken into consideration). It turns out that at the 5% significance level the correlation between PG anomalies and anomalies in temperature or wind velocity is statistically significant (based on the Student's t-test) whereas the analogous correlation for pressure anomalies is not significant.

Computing the multiple linear regression coefficients, we obtain approximately

$$\Delta E\,[\mathrm{V/m}] = -0.51\Delta T\,[^\circ\mathrm{C}] + 2.82\Delta W\,[\mathrm{m/s}],$$

where E is the PG, T is the temperature, W is the wind velocity, and Δ denotes anomalies. Finally, we adjust PG values using these corrections for T and W, namely via the equation

$$E_{\mathrm{adjusted}}\,[\mathrm{V/m}] = E\,[\mathrm{V/m}] - \left(-0.51\,(T - \langle T\rangle)\,[^\circ\mathrm{C}] + 2.82\,(W - \langle W\rangle)\,[\mathrm{m/s}]\right),$$

where angle brackets signify taking the long-term mean value.

Let us note that our adjustment procedure described above is based on similar ideas but not exactly identical to the algorithms employed by Burns et al. (2012) for the earlier Vostok data. They computed anomalies of each variable relative to the 30-day running mean and considered linear regression between these anomalies. In this way they also found out that the correlation with pressure is not statistically significant, and their regression coefficients turned out to be of the same order as ours, albeit somewhat larger (see Burns et al., 2012, equations (9) and (11)). Note, however, that the final adjustments applied in the case of Figure 5b are slightly more complicated, being based on relative PG anomalies and absolute anomalies in meteorological variables (Burns et al., 2012, equations (15)–(18)); in addition, they adjusted these variables to different values compared to our $\langle T\rangle$ and $\langle W\rangle$.

Adjustment of the Vostok potential gradient data for solar wind influences

The variability of Vostok PG values related to solar wind influences is removed in the same manner as the effect of local meteorological factors. First, we compute daily mean values of solar wind imposed potential differences above Vostok calculated with the Weimer 2005 model. Next, we select from the PG data set all formally determined fair-weather days for which solar wind parameters are also available. After that we compute daily anomalies of the PG and solar wind imposed potentials by subtracting the mean values over symmetric 21-day intervals around each day (with only formally selected fine days with solar wind data available taken into consideration). The correlation between PG anomalies and anomalies in solar wind imposed potentials turns out to be very pronounced.

Computing the linear regression coefficient, we obtain

$$\Delta E\,[\mathrm{V/m}] = 0.74\Delta V_{\mathrm{sw}}\,[\mathrm{kV}],$$

where V_{sw} is the solar wind imposed potential difference over Vostok. Finally, we produce the following equation to adjust PG values for E and V_{sw}:

$$E_{\mathrm{adjusted}}\,[\mathrm{V/m}] = E\,[\mathrm{V/m}] - 0.74V_{\mathrm{sw}}\,[\mathrm{kV}];$$

here we adjust PG values to undisturbed conditions (with $V_{\mathrm{sw}} = 0$). Note that our regression coefficient is close to the value earlier reported by Burns et al. (2012, equation (8)).

When we simultaneously adjust the data for local meteorological and solar wind influences, we combine the two formulae in the following way:

$$E_{\mathrm{adjusted}}\,[\mathrm{V/m}] = E\,[\mathrm{V/m}] - \left(-0.51\,(T - \langle T\rangle)\,[^\circ\mathrm{C}] + 2.82\,(W - \langle W\rangle)\,[\mathrm{m/s}] + 0.74V_{\mathrm{sw}}\,[\mathrm{kV}]\right);$$

here we assume the two adjustments to be independent, assuming all relationships to be linear and neglecting possible effects of the solar wind on weather variability.

References

Burns, G. B., Tinsley, B. A., Frank-Kamenetsky, A. V., Troshichev, O. A., French, W. J. R., & Klekociuk, A. R. (2012). Monthly diurnal global atmospheric circuit estimates derived from Vostok electric field measurements adjusted for local meteorological and solar wind influences. *J. Atmos. Sci.*, *69*(6), 2061–2082. doi: 10.1175/JAS-D-11-0212.1

Hersbach, H., Bell, B., Berrisford, P., Biavati, G., Horányi, A., Muñoz Sabater, J., Nicolas, J., Peubey, C., Radu, R., Rozum, I., Schepers, D., Simmons, A., Soci, C., Dee, D., & Thépaut, J.-N. (2023). *ERA5 hourly data on pressure levels from 1940 to present [Dataset].* Copernicus Climate Change Service (C3S) Climate Data Store (CDS). (Accessed on 30 December 2020.) doi: 10.24381/cds.bd0915c6

King, J. H., & Papitashvili, N. E. (2005). Solar wind spatial scales in and comparisons of hourly Wind and ACE plasma and magnetic field data. *J. Geophys. Res.*, *110*(A2), A02104. doi: 10.1029/2004JA010649

Papitashvili, N. E., & King, J. H. (2020). *OMNI hourly data [Dataset].* NASA Space Physics Data Facility. (Accessed on 10 December 2024.) doi: 10.48322/1shr-ht18

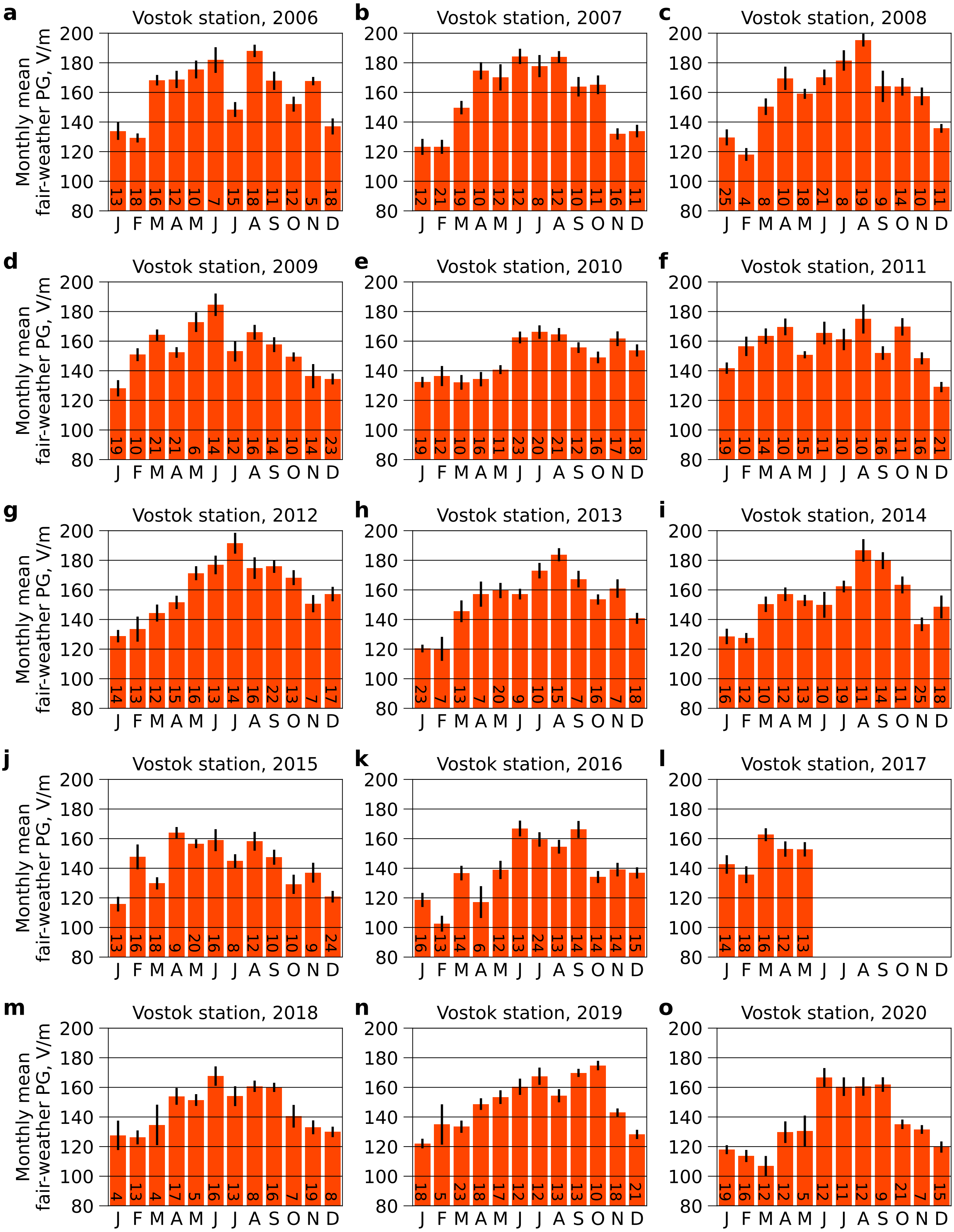

Figure S1. (a)–(o) Monthly mean values of the fair-weather PG according to measurements at the Vostok station for each individual year within 2006–2020. Annotations inside the bars in all panels indicate the number of fair-weather days used to calculate the average values. Error bars demonstrate the values plus and minus one standard error. The absent bars in panel (l) correspond to a gap in the data.

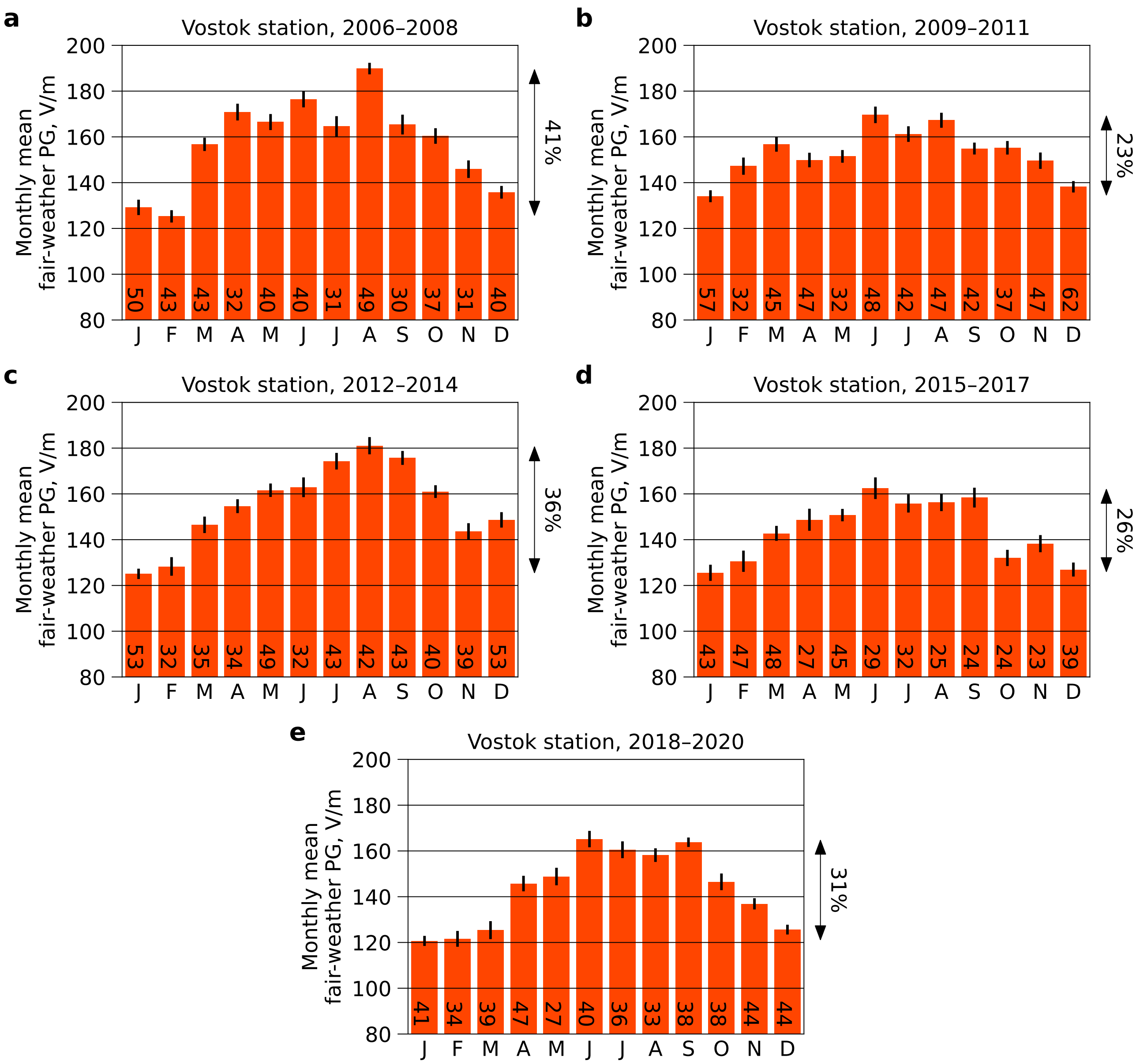

Figure S2. (a)–(e) Monthly mean values of the fair-weather PG according to measurements at the Vostok station for 3-year periods within 2006–2020. Annotations inside the bars in all panels indicate the number of fair-weather days used to calculate the average values. Error bars demonstrate the values plus and minus one standard error. The double arrow to the right of each panel represents the peak-to-peak amplitude, and the number next to it gives this amplitude as a fraction of the annual mean.

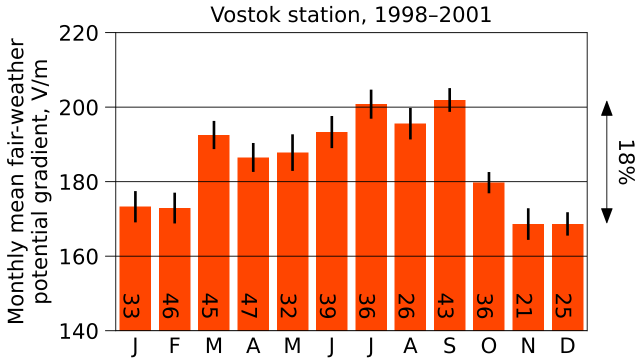

Figure S3. Monthly mean values of the fair-weather PG according to measurements at the Vostok station in 1998–2001 (analyzed using the same procedure which we applied for the 2006–2020 data set). Annotations inside the bars indicate the number of fair-weather days used to calculate the average values. Error bars demonstrate the values plus and minus one standard error. The double arrow to the right of the bar plot represents the peak-to-peak amplitude, and the number next to it gives this amplitude as a fraction of the annual mean.

Powers, J. G., Klemp, J. B., Skamarock, W. C., Davis, C. A., Dudhia, J., Gill, D. O., Coen, J. L., Gochis, D. J., Ahmadov, R., Peckham, S. E., Grell, G. A., Michalakes, J., Trahan, S., Benjamin, S. G., Alexander, C. R., Dimego, G. J., Wang, W., Schwartz, C. S., Romine, G. S., Liu, Z., Snyder, C., Chen, F., Barlage, M. J., Yu, W., & Duda, M. G. (2017). The Weather Research and Forecasting model: Overview, system efforts, and future directions. *Bull. Amer. Meteor. Soc.*, *98*(8), 1717–1737. doi: 10.1175/BAMS-D-15-00308.1

Skamarock, W. C., Klemp, J. B., Dudhia, J., Gill, D. O., Liu, Z., Berner, J., Wang, W., Powers, J. G., Duda, M. G., Barker, D. M., & Huang, X.-Y. (2019). *A description of the Advanced Research WRF Version 4* (NCAR Technical Note NCAR/TN-556+STR). doi: 10.5065/1dfh-6p97

Weimer, D. (2019). *Weimer 2005 ionospheric electric potential model for IDL [Software].* Zenodo. doi: 10.5281/zenodo.2530324

Weimer, D. R. (2005a). Improved ionospheric electrodynamic models and application to calculating Joule heating rates. *J. Geophys. Res.*, *110*(A5), A05306. doi: 10.1029/2004JA010884

Weimer, D. R. (2005b). Predicting surface geomagnetic variations using ionospheric electrodynamic models. *J. Geophys. Res.*, *110*(A12), A12307. doi: 10.1029/2005JA011270